Geochemistry Geophysics Geosystems G3
AN ELECTRONIC JOURNAL OF THE EARTH SCIENCES
Published by AGU and the Geochemical Society

*Article*
Volume 9, Number 10
9 October 2008
Q10S10, doi:10.1029/2008GC002040
ISSN: 1525-2027

# Strong along-arc variations in attenuation in the mantle wedge beneath Costa Rica and Nicaragua

**C. A. Rychert**
*Institute of Geophysics and Planetary Physics, Scripps Institution of Oceanography, University of California, San Diego, 9500 Gilman Drive, La Jolla, California 92093-0225, USA (crychert@ucsd.edu)*

**K. M. Fischer**
*Department of Geological Sciences, Brown University, 324 Brook Street, Box 1846, Providence, Rhode Island 02912, USA*

**G. A. Abers and T. Plank**
*Lamont-Doherty Earth Observatory, PO Box 1000, 61 Route 9W, Palisades, New York 10964, USA*

**E. Syracuse**
*Department of Earth Sciences, Boston University, 675 Commonwealth Avenue, Boston, Massachusetts 02215, USA*

**J. M. Protti and V. Gonzalez**
*Observatorio Vulcanológico y Sismológico de Costa Rica, Universidad Nacional, Apartado 2346-3000 Heredia, Costa Rica*

**W. Strauch**
*Department of Geophysics, Instituto Nicaraguense de Estudios Territoriales, Apartado 2110, Managua, Nicaragua*

[1] Attenuation structure in the Central American subduction zone was imaged using local events recorded by the Tomography Under Costa Rica and Nicaragua array, a 20-month-long deployment (July 2004 until March 2006) of 48 seismometers that spanned the fore-arc, arc, and back-arc regions of Nicaragua and Costa Rica. *P* and *S* waveforms were inverted separately for the corner frequency and moment of each event and for the path-averaged attenuation operator ($t^*$) of each event-station pair, assuming attenuation is slightly frequency-dependent ($\propto = 0.27$). Then, tomographic inversions were performed for *S* and *P* attenuation ($Q_S^{-1}$ and $Q_P^{-1}$). Since *P* wave amplitudes reflect both shear and the bulk moduli, tomographic inversions were also performed to determine shear and bulk attenuation ($Q_S^{-1}$ and $Q_\kappa^{-1}$), the loss of energy per cycle owing to shearing and uniform compression, respectively. Damping and other inversion tomographic parameters were systematically varied. As is typical in subduction zone attenuation studies, a less attenuating slab, upper plate, and wedge corner and a more attenuating mantle wedge were imaged. In addition, first-order differences between the mantles beneath Nicaragua and Costa Rica were observed. The slab in Nicaragua is more attenuating than the slab in Costa Rica. A larger zone of higher shear attenuation also characterizes the Nicaraguan mantle wedge. Within the wedge, maximum attenuation values at 1 Hz correspond to $Qs = 38–73$ beneath Nicaragua and $Qs = 62–84$ beneath Costa Rica, and average values are $Qs = 76–78$ and $Qs = 84–88$, respectively. Attenuation variations correlate with along-arc trends in geochemical indicators that suggest that melting beneath Nicaragua occurs at more hydrated conditions, and possibly to greater extents and depths, relative to northern Costa Rica. Shear attenuation dominates over bulk attenuation in the well-resolved regions of the wedge. The more extensive zones of greater shear attenuation observed in the Nicaraguan wedge could be explained by higher temperatures

Copyright 2008 by the American Geophysical Union

and/or greater hydration, but comparison with petrological data suggests that hydration variations play a larger role. Average wedge attenuation values are comparable to estimates for the Andes and Japan, greater than those for Alaska, and less than those for Tonga-Lau.

**Components:** 15,590 words, 11 figures, 2 tables.

**Keywords:** Central America; subduction; attenuation; mantle wedge; hydration; melting.

**Index Terms:** 8170 Tectonophysics: Subduction zone processes (1031, 3060, 3613, 8413); 7270 Seismology: Tomography (6982, 8180); 7203 Seismology: Body waves.

**Received** 29 March 2008; **Revised** 27 July 2008; **Accepted** 12 August 2008; **Published** 9 October 2008.

Rychert, C. A., K. M. Fischer, G. A. Abers, T. Plank, E. Syracuse, J. M. Protti, V. Gonzalez, and W. Strauch (2008), Strong along-arc variations in attenuation in the mantle wedge beneath Costa Rica and Nicaragua, *Geochem. Geophys. Geosyst.*, *9*, Q10S10, doi:10.1029/2008GC002040.

**Theme:** Central American Subduction System
**Guest Editors:** G. Alvarado, K. Hoernle, and E. Silver

## 1. Introduction

[2] It is widely accepted that the downgoing slab transports volatiles into the Earth that enable melting and volcanism in subduction zones by lowering the melting temperature of the mantle wedge. However, the factors that control melting dynamics are not well understood. Is the wedge hydrated throughout with thermal structure and flow pattern dictating melt initiation and mobility? Or, is the distribution of volatiles from the slab the controlling factor? What controls the extent of melting? Does volatile content, the thermal structure of the wedge, or the distance available for decompression melting dominate? Globally, subduction zone melting is most likely complicated by several of these mechanisms working either together or in different sections of the wedge [*Tatsumi*, 1986; *Spiegelman and McKenzie*, 1987; *Plank and Langmuir*, 1988; *Furukawa*, 1993; *Stolper and Newman*, 1994; *Iwamori*, 1997; *Schmidt and Poli*, 1998; *Kelemen et al.*, 2003; *Peacock et al.*, 2005; *Wallace*, 2005; *Grove et al.*, 2006; *Kelley et al.*, 2006; *Langmuir et al.*, 2006]. Attenuation tomography in Cost Rica and Nicaragua provides a partial but integral piece of the melting dynamics puzzle by helping to constrain the thermal structure and the role of volatiles in two wedge regions that are close in geographical proximity but poles apart in terms of melting characteristics.

[3] Understanding melting dynamics in subduction zones requires integration of many types of data and analyses that are not always available in parallel. For instance, in some subduction zones seismic station spacing has been too sparse to fully test melting hypotheses. Conversely, in some regions where seismic resolution is excellent geochemical signatures of wedge melting are strongly overprinted by the upper plate, as in Japan [*Gust et al.*, 1997; *Tsumura et al.*, 2000; *Nakajima et al.*, 2005], or a lack of active volcanism inhibits sampling of current mantle conditions, as in central Alaska [*Stachnik et al.*, 2004].

[4] Attenuation structure in Costa Rica and Nicaragua offers a unique opportunity to test melting hypotheses. The arc chemistry represents contributions from the subducting slab and melting mantle, without significant overprinting from the upper plate [*Carr et al.*, 2003]. In addition, geochemical variations are systematic along the arc (Figure 1), and represent global extremes. Furthermore, the Tomography Under Costa Rica and Nicaragua (TUCAN) deployment of 48 seismometers from July 2004 until March 2006 offers an ideal geometry to probe the origin of the geochemical observations (Figure 1). The array consisted of two arc-perpendicular lines with ~10 km station spacing and two arc-parallel lines with ~50 km station spacing, providing high-resolution imaging across the arc close to where end-member geochemical signatures are observed, in northwestern Nicaragua and northwestern Costa Rica, as well as good resolution of variations along the arc. Finally, seismic attenuation is strongly dependent on temperature, and experimental results allow attenuation values to be translated directly into temperature [*Jackson et al.*, 2002; *Nakajima and Hasegawa*, 2003; *Faul and Jackson*, 2005]. Attenuation may



15252027, 2008, 10, Downloaded from https://agupubs.onlinelibrary.wiley.com/doi/10.1029/2008GC002040 by Cochrane Costa Rica, Wiley Online Library on [21/07/2025]. See the Terms and Conditions (https://onlinelibrary.wiley.com/terms-and-conditions) on Wiley Online Library for rules of use; OA articles are governed by the applicable Creative Commons License

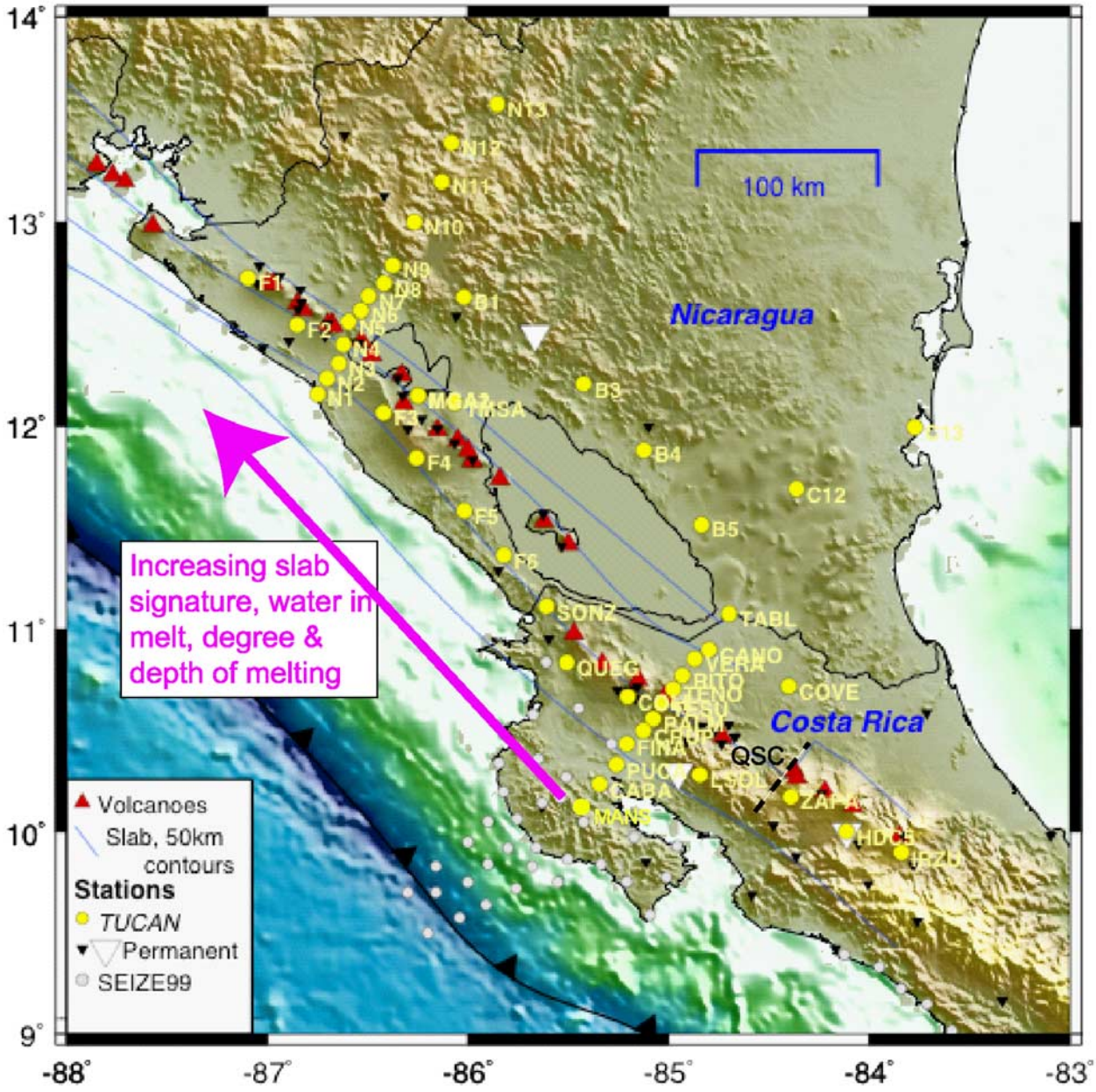


**Figure 1.** Map of the study region. Shading indicates topography. The black line with triangles marks the trench. Red triangles mark volcanoes. Yellow circles mark the Tomography Under Costa Rica and Nicaragua (TUCAN) broadband seismic array. White and black inverted triangles mark permanent stations. White circles mark Seismogenic Zone Experiment (SEIZE) array. Slab contours are shown with blue line. Black dashed line traces the Quesada Sharp Contortion (QSC) [*Protti et al.*, 1995]. Purple arrow denotes direction of increases in geochemical indicators of water content and degree and depth of melting [*Plank and Langmuir*, 1988; 1993; *Leeman et al.*, 1994; *Reagan et al.*, 1994; *Roggensack et al.*, 1997; *Patino et al.*, 2000; *Carr et al.*, 2003; *Kelley et al.*, 2006; *Sadofsky et al.*, 2008].

also reflect other factors such as the presence of volatiles [*Karato*, 2003; *Aizawa et al.*, 2008] and melt [*Jackson et al.*, 2004], complicating interpretations to some degree but also offering important insight regarding the location of volatiles and/or melt. The relationship between the high-resolution attenuation information provided by the TUCAN array to the relatively simple, yet strong, geochemical variations has the potential to illuminate volatile and temperature anomalies, and aid in determining the factors that control melting dynamics in subduction zones.



15252027, 2008, 10, Downloaded from https://agupubs.onlinelibrary.wiley.com/doi/10.1029/2008GC002040 by Cochrane Costa Rica, Wiley Online Library on [21/07/2025]. See the Terms and Conditions (https://onlinelibrary.wiley.com/terms-and-conditions) on Wiley Online Library for rules of use; OA articles are governed by the applicable Creative Commons License

## 1.1. Tectonic Setting

[5] The properties of the subducting Cocos Plate vary only modestly along the portion of the Nicaragua-Costa Rica subduction zone sampled by the TUCAN array. The rate of convergence ranges from 75 mm $a^{-1}$ in Nicaragua to 90 mm $a^{-1}$ in Costa Rica with a maximum trench-parallel component of ~14 mm $a^{-1}$ in Nicaragua [*DeMets*, 2001]. The age of the downgoing crust only varies from ~24 Ma to 16 Ma [*Barckhausen et al.*, 2001]. A shift in the roughness of the downgoing plate has been well documented [*von Huene et al.*, 2000; *Ranero et al.*, 2003], but all except the three most southern TUCAN stations are located northwest of this boundary, where the Cocos plate is relatively smooth and contains no large seamounts. On the other hand, the slab entering the trench in Nicaragua is characterized by normal faults with graben offsets of up to 500 m; normal faulting in the downgoing plate is also observed in the subducting plate segment just to the south of the rough-smooth boundary [*Ranero et al.*, 2003]. More dramatic tectonic variations occur between Nicaragua and Costa Rica when the upper plate is considered. Most obviously, the volcanoes in Nicaragua are offset from those in Costa Rica by ~40 km (Figure 1). Directly beneath the arc and along our seismic lines, slab earthquakes are observed at depths as shallow as ~160 km beneath Nicaragua and ~85 km beneath northwestern Costa Rica [*Syracuse and Abers*, 2006] in agreement with body-wave tomography that also utilized data from the TUCAN experiment [*Syracuse et al.*, 2008].

[6] The compositions of the upper plates of Costa Rica and Nicaragua also vary. Much of the back arc of Nicaragua is made up of the Chortis block, which is believed to have a basement of continental type [*Donnelly et al.*, 1990], while the Pacific coast is an accreted terrane [*Case et al.*, 1990] that is possibly a relict arc [*Walther*, 2000]. The Chorotega block in Costa Rica is mainly composed of mafic igneous rocks of oceanic origin [*Escalante*, 1990; *Sinton et al.*, 1997]. These terranes are reflected in crustal *P* wave/*S* wave velocity ratios in data from the TUCAN experiment that show lower values in the more silicic Chortis block and higher values in the more mafic Chortega block [*MacKenzie et al.*, 2008].

## 1.2. Along-Arc Geochemical Variations

[7] A variety of strong along-arc variations in the composition of arc magmas have been well-documented. Overall, geochemical tracers of the slab (Ba/La, B/La, and $^{10}$Be) peak globally in Nicaragua and decrease to a global minimum at the arc terminus in Costa Rica [*Carr et al.*, 1990; *Morris et al.*, 1990; *Leeman et al.*, 1994]. The implications of the trace element variations, however, are not entirely clear. They could represent more fluids from the slab in Nicaragua, but other factors include variation in the amount and type of subducted sediment, heterogeneity in the subducted and upper plate crust and mantle, and/or variable degrees of melting in the wedge [*Leeman et al.*, 1994; *Werner et al.*, 1999; *Hoernle et al.*, 2000; *Patino et al.*, 2000; *Carr et al.*, 2003; *Eiler et al.*, 2005; *Wade et al.*, 2006; *Benjamin et al.*, 2007; *Sadofsky et al.*, 2008].

[8] In order to better constrain the source of the geochemical variations, much recent effort has focused on the measurement of $H_2O$ itself in undegassed melt inclusions from Central American volcanoes. Melt inclusions show evidence for water-fluxed melting everywhere along the arc, but the highest magmatic water contents (up to 6%) are measured in Cerro Negro basaltic melt inclusions, near the dense arc-normal line of TUCAN stations in Nicaragua, with lower water contents of only 3–4% in northern and central Costa Rica melt inclusions [*Roggensack et al.*, 1997; *Wade et al.*, 2006; *Benjamin et al.*, 2007; *Sadofsky et al.*, 2008]. The one exception are locally high water contents in some inclusions from Irazu volcano in central Costa Rica, but processes here may be anomalous due to the influence of subducted hot spots and/or the Cocos ridge [*Benjamin et al.*, 2007; *Sadofsky et al.*, 2008], and Irazu lies largely outside of the resolution of our array. Nonetheless, Irazu provides one common example of the large local variability that exists in the water content of magmas erupted closely in space and time. For example, some Nejapa cinder cones (not far from Cerro Negro in Nicaragua) erupt relatively dry magmas (<3 wt % $H_2O$), while Grenada cinder cones in southeast Nicaragua erupt both wet (>4 wt % $H_2O$) and drier (<3 wt % $H_2O$) magmas [*Sadofsky et al.*, 2008]. Thus, given the local variability that exists, and the fact that only ~5 volcanoes have yet to yield useful (undegassed) $H_2O$ measurements, it may be premature to generalize results regionally, at a scale relevant to the seismic observables. On the other hand, both the works of *Wade et al.* [2006] and *Sadofsky et al.* [2008] have pointed out that $H_2O$ and Ba/La correlate among the melt inclusions population, and we will make use of this later to develop preliminary regional averages in magmatic, and mantle, water contents. Such a view clearly



15252027, 2008, 10, Downloaded from https://agupubs.onlinelibrary.wiley.com/doi/10.1029/2008GC002040 by Cochrane Costa Rica, Wiley Online Library on [21/07/2025]. See the Terms and Conditions (https://onlinelibrary.wiley.com/terms-and-conditions) on Wiley Online Library for rules of use; OA articles are governed by the applicable Creative Commons License

predicts higher water contents in the mantle on average beneath Nicaragua than beneath Costa Rica.

[9] While our understanding of the distribution of water in Central American magmas is still developing, other evidence points to greater and/or deeper hydration of the subducting plate beneath Nicaragua. This includes deep normal faults observed in the Cocos plate before it subducts [*Ranero et al.*, 2003], low crust and mantle velocities in the subducting plate seaward of the trench consistent with 12–17% mantle serpentinization [*Ivandic et al.*, 2008], an unusually thick low velocity layer sensed by body waves trapped near the slab-wedge interface [*Abers et al.*, 2003], and a mantle-penetrating low velocity layer indicative of 10–20% serpentine constrained by body wave tomography with TUCAN array data [*Syracuse et al.*, 2008]. Such geophysical evidence for deeper hydration of the Nicaraguan slab is also consistent with the anomalously low $\delta^{18}O$ values that are found in Nicaraguan olivines, relative to those in Costa Rica or any other arc olivine globally [*Eiler et al.*, 2005]. Such low values require high-temperature hydrothermal reactions such as might occur in deeper regions of the subducting plate. Thus, taken together, the trace element, isotopic, geophysical, and preliminary $H_2O$ data point to a greater hydration of the Nicaraguan slab, mantle, and magmas.

[10] In addition to what appears to be an along-arc variation in water input, other along-arc changes in slab and wedge physical conditions may also play a role in dehydration and melting processes. Previously considered factors include along-arc variations in slab dip [e.g., *Carr et al.*, 1990, 2003, 2007] and temperature [e.g., *Leeman et al.*, 1994; *Chan et al.*, 1999; *Peacock et al.*, 2005]. In addition, northwestern along-arc transport of mantle wedge material has been proposed [*Herrstrom et al.*, 1995; *Abratis and Woerner*, 2001; *Hoernle et al.*, 2008] which could produce wedge material beneath northwestern Nicaragua that has a longer history of interaction with the Cocos plate and a stronger slab signature.

[11] Despite the preceding evidence for greater hydration in the Nicaraguan mantle wedge, the link between volatile abundance and magmatic productivity is unclear. Along-arc variations in Ca, Na, Fe, and Si are consistent with a greater degree of melting in Nicaragua than in Costa Rica, and some evidence exists for greater pressures of melt equilibration beneath Nicaragua as well [*Plank and Langmuir*, 1988; *Langmuir et al.*, 1992; *Carr et al.*, 2003; *Sadofsky et al.*, 2008]. Such higher degrees of melting would be consistent with higher water contents driving melting [*Kelley et al.*, 2006; *Langmuir et al.*, 2006; *Sadofsky et al.*, 2008]. However, estimates of extrusive volcanic flux based on volcanic edifices are similar between Nicaragua and Costa Rica [*Carr et al.*, 2007], although when tephra volumes are included, magma flux in Nicaragua may be somewhat higher than in Costa Rica [*Kutterolf et al.*, 2008]. Thus, while there may be a link between the $H_2O$ content of the mantle and degree of melting, the link with magma production is less clear.

[12] In order to provide new constraints on these questions that relate to the melting process in the mantle, we use attenuation tomography to probe the structure of the slab and wedge and constrain the distribution of water and temperature in the subduction zone.

## 2. Methods

### 2.1. Calculating *t**

[13] The spectra of *P* and *S* waveforms from local events recorded by the TUCAN array were analyzed using the vertical and transverse components, respectively, following the method of *Stachnik et al.* [2004]. *P* and *S* arrivals were picked on waveform time series [*Syracuse et al.*, 2008], then multitaper spectra [*Park et al.*, 1987] were calculated in 3-s windows, starting 0.5 s before the arrival, corrected for instrument gain, and converted to displacement (Figure 2). Signal-to-noise ratios (SNRs) were determined using the noise spectra calculated from a 3-s window before each of the signals.

[14] Path-averaged attenuation was parameterized in terms of an attenuation operator, $t^* = \tau/Q$, for travel time $\tau$ assuming a displacement spectrum $A_{jk}(f_i)$ as follows:

$$A_{jk}(f_i) = C_{jk} M_{0k} e^{-\pi f_i t^*_{jk}} / (1 + (f_i/f_{ck})^2) \quad (1)$$

[e.g., *Anderson and Hough*, 1984] for the *k*th event recorded at the *j*th station for each frequency ($f_i$), where $C_{jk}(r)$ is a constant accounting for frequency-independent effects of each path, such as geometrical spreading, free surface interaction, and the spherical average of the radiation pattern [*Aki and Richards*, 1980]. $M_{0k}/(1 + (f_i/f_{ck})^2)$ is a simple source spectrum [*Brune*, 1970] where $M_{0k}$ and $f_{ck}$ are the seismic moment and corner frequency, allowing a different seismic moment and corner



15252027, 2008, 10, Downloaded from https://agupubs.onlinelibrary.wiley.com/doi/10.1029/2008GC002040 by Cochrane Costa Rica, Wiley Online Library on [21/07/2025]. See the Terms and Conditions (https://onlinelibrary.wiley.com/terms-and-conditions) on Wiley Online Library for rules of use; OA articles are governed by the applicable Creative Commons License

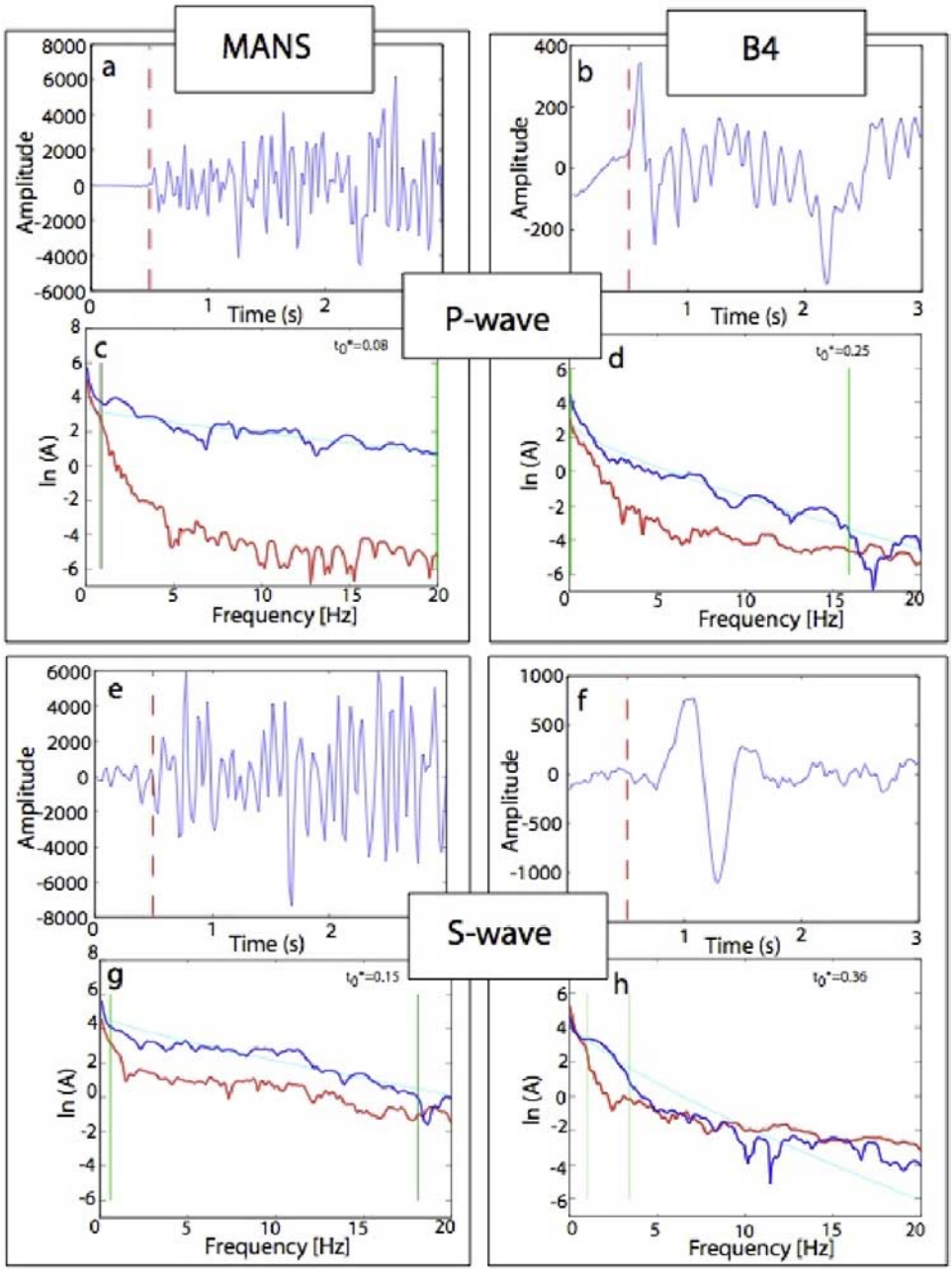


**Figure 2.** Waveform and spectrum examples. (a, b, e, f) Waveforms and (c, d, g, h) corresponding spectra of both the *P* wave (Figures 2a–2d) and the *S* wave (Figures 2e–2h) are compared at a station in the fore arc, MANS (Figures 2a, 2c, 2e, and 2g), and a station in the back arc, B4 (Figures 2b, 2d, 2f, and 2h). The hypocenter of the event was at 109 km depth, 10.6°N, −84.8°W, i.e., in the slab, beneath the arc near the Costa Rica line of the TUCAN array. In the waveform plots the blue lines represent the signal, and the dashed red lines are the picks on the signals. In the spectrum plots, blue lines represent the spectra, red lines represent noise, and cyan lines show the best fitting spectra from the $t^*$ inversions. Green vertical lines delimit the frequencies that are used in the inversion for $t^*$.

frequency for the *P* and *S* wave of each earthquake. The equation was rearranged into the following form:

$$\ln(A_{jk}(f_i)) + \ln(1 + (f_i/f_{ck})^2) - \ln(C_{jk}(r)) = \ln(M_{0k}) - \pi f_i t^*_{jk} \quad (2)$$

[*Stachnik et al.*, 2004]. Equation (2) was then solved for a single corner frequency and moment for each event and an attenuation operator for each event-station pair, for both *P* and *S* waveforms. Since the problem is nonlinear, the equation was



15252027, 2008, 10, Downloaded from https://agupubs.onlinelibrary.wiley.com/doi/10.1029/2008GC002040 by Cochrane Costa Rica, Wiley Online Library on [21/07/2025]. See the Terms and Conditions (https://onlinelibrary.wiley.com/terms-and-conditions) on Wiley Online Library for rules of use; OA articles are governed by the applicable Creative Commons License

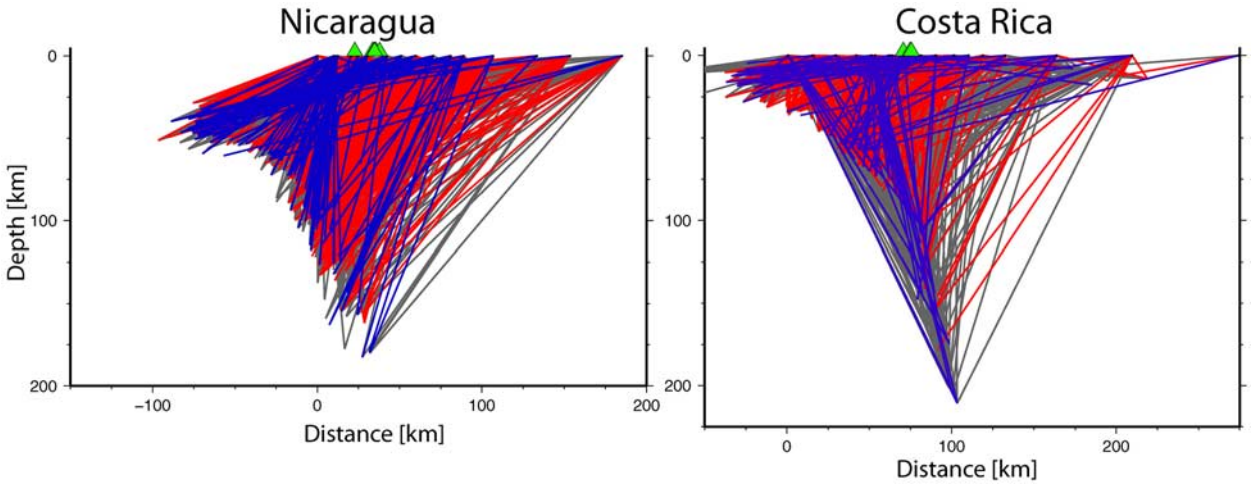


**Figure 3.** Path-averaged attenuation values from *S* spectra. Blue, red, and gray lines represent low ($Q_S > 600$), high ($Q_S < 100$), and intermediate ($Q_S > 600$, $Q_S < 100$) path-averaged attenuation respectively. Projection width is 50 km on each side of the cross section. Green triangles mark volcano locations.

solved by performing a grid search over $f_c$, testing values from 0.25 to 50 Hz at 0.25 Hz intervals, and then linearly inverting for $M_{0k}$ and $t^*_{jk}$.

[15] Experimental results indicate that attenuation is frequency-dependent [*Jackson et al.*, 2002; *Faul and Jackson*, 2005], and this assumption was implemented here according to the following equation:

$$t^* \equiv t_0^* f^{-\alpha} \tag{3}$$

substituting $t^*$ from equation (3) into equation (2), and solving for $t_0^*$, the path-averaged attenuation operator at 1 Hz [*Stachnik et al.*, 2004]. The frequency dependence of attenuation was chosen according to experimental results ($\alpha$ = 0.27) [*Jackson et al.*, 2002; *Stachnik et al.*, 2004]. The effects of this assumption are described in section 2.3.

[16] *P* and *S* waveform examples and their corresponding $t_0^*$ values from an earthquake in the slab at a depth of 109 km (Figure 2) show dramatically greater attenuation on paths that cross the mantle wedge (back-arc station B4) than those that lie within or close to the slab (fore-arc station MANS). Source parameters and $t_0^*$ values are obtained by fitting data only where signal exceeds 2.5 times the background noise (shown by solid, green, vertical bars in the Figure 2 spectra). Path-averaged $Q_S$ values from $t_S^*$ values (Figure 3) provide a first-order indication of low $Q_S^{-1}$ slab and upper plate regions, a high $Q_S^{-1}$ wedge beneath the arc and back arc, and intermediate $Q_S^{-1}$ values in the shallow wedge corner.

## 2.2. Data Selection

[17] Data processing and selection generally follow the work of *Stachnik et al.* [2004]; the main difference is that the spectra presented here were automatically windowed. However, many of the same rules were applied. For instance, only earthquakes with useable spectral windows on both *P* and *S* waveforms were employed. Also, only one frequency band was picked out of a given spectrum. Finally, as previously mentioned, the band must have SNR $\geq$ 2.5.

[18] For the automatic picking, the low-frequency cutoff must be $\leq$10 Hz and the highest frequency must be $\leq$20 Hz. If multiple bands satisfy picking criteria in this range, i.e., multiple bands with SNR $\geq$ 2.5 separated by bands with SNR $\leq$ 2.5, the lower-frequency band was chosen as long as it was at least 1/3 the length of any band at higher frequencies and it was longer than 1 Hz. If that was not the case, the second, higher-frequency band was chosen. If no frequency band exists that is longer than 1 Hz with SNR $\geq$ 2.5 for either the *P* or the *S* wave at a given station, the signal was not used in the inversion. There are two benefits to only using signals where both *P* and *S* have frequency bands that satisfy the acceptance criteria. First, requiring that useable *P* and *S* bands exist is a good way to select only the highest-quality events. Second, the restriction leads to comparable resolution in the *P* and *S* wave attenuation results. This is an important factor when comparing *P* and *S* models and is particularly useful when constraining bulk attenuation. All negative $t^*$ measurements were



15252027, 2008, 10, Downloaded from https://agupubs.onlinelibrary.wiley.com/doi/10.1029/2008GC002040 by Cochrane Costa Rica, Wiley Online Library on [21/07/2025]. See the Terms and Conditions (https://onlinelibrary.wiley.com/terms-and-conditions) on Wiley Online Library for rules of use; OA articles are governed by the applicable Creative Commons License

excluded from the tomographic inversions, as well as all events for which greater than 50% of the $t^*$ measurements are negative, since they are likely poor quality. This data exclusion was done separately for both $P$ and $S$ wave measurements and left 1097 $S$ and 1105 $P$ events and 9136 $S$ and 9630 $P$ station-event pairs. We also tested the case where the same event-station pairs were excluded for $P$ and $S$, as described in greater detail in section 4.2.

## 2.3. Testing $t^*$ Inversion Assumptions

[19] We examined how the $t^*$ values were affected by (1) inverting for corner frequency, (2) including data at the upper end of the chosen frequency band, and (3) assuming frequency-dependent attenuation.

[20] The ability to resolve corner frequency as an inversion parameter was tested by performing $t^*$ inversions with corner frequency fixed at 40 Hz, in effect assuming that all earthquakes are too small for source properties to affect spectral falloff. Using an $F$ test for significance of regression, the resulting fits to the observed spectra were compared to those from the case in which corner frequency was an inversion parameter. The $F$ value of this result was 12.80, exceeding 1.08, the $F$ value required for 95% confidence. Thus, $t^*$ values using the best fitting corner frequencies provide significantly better fits to the data, and these are the measurements used in the preferred inversions for attenuation. Most corner frequencies in our results are <20 Hz. However, we do allow corner frequency to vary up to 50 Hz, since corner frequencies in this range also affect the shape of spectra at the frequencies used in our inversion (<20 Hz) according to equation (1).

[21] The usefulness of information at frequencies greater than 6 Hz was tested, since in several cases spectra were too attenuated to attain any usable information at higher frequencies. (See, for example, the $S$ wave spectrum at station B4 in Figure 2.) When higher frequencies were excluded regardless of SNR, the best fitting corner frequencies that were previously in the 10–20 Hz range became extreme values, either smaller (0–5 Hz) or larger (45–50 Hz, the maximum allowed). While the overall character of the tomographic inversions assuming a limited frequency band remained the same, model length increased. This is a logical result, i.e., a loss of information in the upper frequency band leads to inaccurate, extreme corner frequency estimates, and consequently, less stable attenuation operators. Thus, all frequencies that satisfy SNR criteria as described in section 2.2 are included in the final attenuation results.

[22] The ability to resolve the frequency dependence of attenuation was tested by performing $t^*$ inversions without it ($\alpha = 0$). By including frequency dependence, the work of *Stachnik et al.* [2004] found that the variance in the $t^*$ measurements for the spectra of wedge paths was reduced by ~10% with $\alpha = 0.27$ and by ~14% with their best fitting frequency dependence, $\alpha = 0.4–0.5$. This result is also consistent with experimental results that indicate that attenuation is frequency-dependent [*Jackson et al.*, 2002; *Faul and Jackson*, 2005]. Variance in the Central America wedge paths was reduced by 1% by including frequency dependence ($\alpha = 0.27$), an insignificant amount according to the $F$ test. However, since the best fitting path-averaged $t^*$ model included frequency-dependent attenuation ($\alpha = 0.27$), and since frequency dependence enables comparison with experimental results, this assumption is included in the final attenuation models.

## 2.4. Tomographic Inversion

[23] Tomographic inversions of both $P$ and $S$ wave path-averaged attenuation operators ($t_P^*$ and $t_S^*$) were performed to determine attenuation structure. Direct inversions of $t_P^*$ for $Q_P^{-1}$ and $t_S^*$ for $Q_S^{-1}$ were carried out using the approach of *Stachnik et al.* [2004]. In addition, joint inversions of $t_P^*$ and $t_S^*$ for either shear attenuation, assuming $Q_\kappa^{-1}$ is negligible, or for $Q_\kappa^{-1}$ and $Q_S^{-1}$ were performed.

[24] Following the work of *Stachnik et al.* [2004], the forward problem is represented as:

$$t_i^* = \sum_j l_{ij}/V_j Q_j \tag{4}$$

where $l_{ij}$ is the path length of the $i$th ray in the $j$th block, and $V_j$ and $1/Q_j$ are the velocity and attenuation of block $j$. Block velocities are the same as those used in the ray tracing, and are very similar to the best fitting one-dimensional (1-D) model for the region [*Syracuse et al.*, 2008], within 2%. In the joint inversions of $t_S^*$ and $t_P^*$ for $Q_S^{-1}$ and $Q_\kappa^{-1}$, the following equations were used to relate $Q_P^{-1}$ to $Q_S^{-1}$ and $Q_\kappa^{-1}$:

$$1/Q_p = (1 - L)/Q_\kappa + L/Q_S \tag{5}$$



15252027, 2008, 10, Downloaded from https://agupubs.onlinelibrary.wiley.com/doi/10.1029/2008GC002040 by Cochrane Costa Rica, Wiley Online Library on [21/07/2025]. See the Terms and Conditions (https://onlinelibrary.wiley.com/terms-and-conditions) on Wiley Online Library for rules of use; OA articles are governed by the applicable Creative Commons License

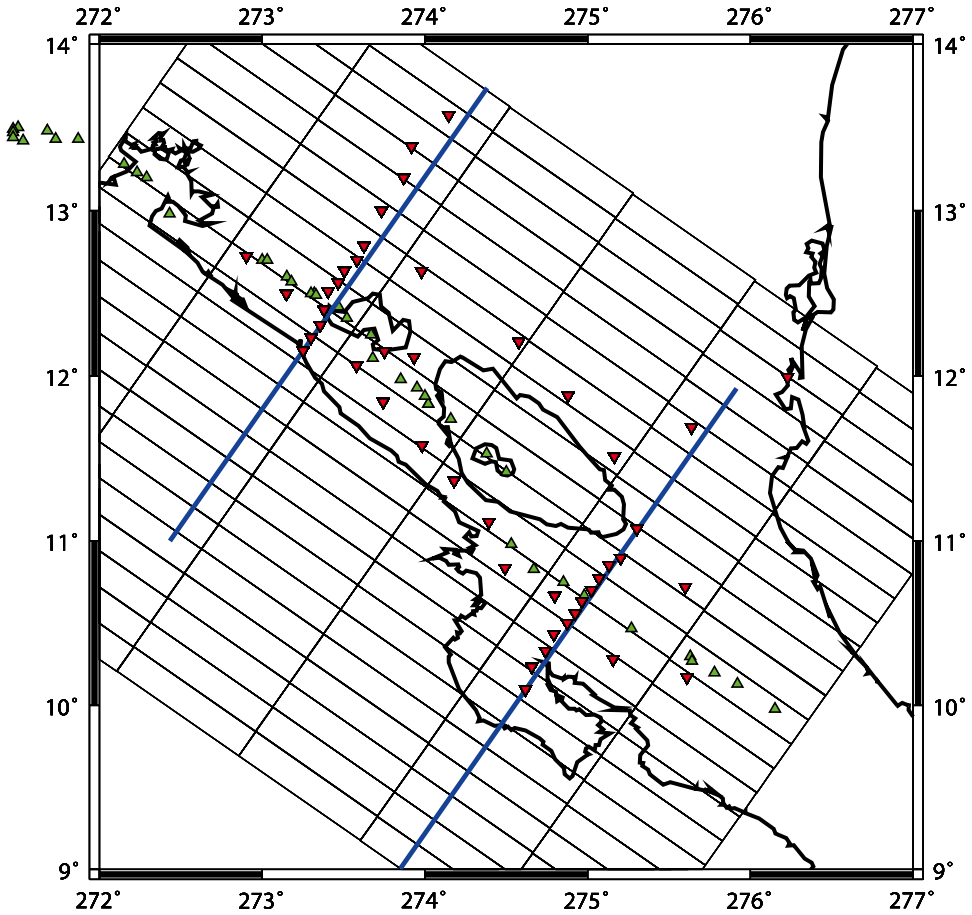


**Figure 4.** Block parameterization. The blocks outlined in black represent those used to parameterize 3-D space in all layers below the top 500 m in all of the inversions for attenuation structure except for the minimum parameterization inversions. The blocks are 20 km across strike, 100 km along strike, and 20 km in depth. The blocks are angled at an azimuth of 35°. Blue lines are the lines along which all cross sections are projected, southwest to northeast here corresponding to left to right in cross section. The Nicaragua cross-section line is the one in the northwest and the Costa Rica line is the one in the southeast. The stations are marked by inverted red triangles. Volcanoes are marked by green triangles. Black lines outline the coast.

where

$$L = (4/3)(V_S/V_P)^2$$

[e.g., *Anderson*, 1989].

[25] The $t^*$ data were inverted with a maximum likelihood linear inverse solution [*Tarantola and Valette*, 1982], using a 1-D a priori estimate of $Q^{-1}$, a priori covariance of the data from the $t^*$ inversions, a priori covariance of the model, and a priori covariance of the theoretical uncertainty. In all results and resolution tests presented here, unless otherwise noted, the 1-D a priori starting model, $m_0$, is $Q_S = 600$ and $Q_\kappa = 3000$ in the crust and mantle. $Q_S = 25$ and $Q_\kappa = 25$ from 0 to 500 m depth, allowing for a lossy near surface layer [*Hough and Anderson*, 1988; *Abercrombie*, 1997; *Stachnik et al.*, 2004].

[26] Unless otherwise noted, uncertainty in the a priori model was assumed to be 100% of the starting model. Uncertainty in theory [*Tarantola*, 1987] was assumed to be 0.03 s, based on past estimates of otherwise unmodeled errors in $t^*$ [*Sarker and Abers*, 1998; *Stachnik et al.*, 2004]. For example, uncertainty in theory includes uncertainty in the chosen source model, and also additional error associated with $f_c$, since the a priori covariance of the data only reflects the error in the linear part of the inversion for $t^*$. The uncertainty in theory was determined from variations in $t^*$ between collocated events [*Stachnik et al.*, 2004].

[27] The Nicaragua-Costa Rica subduction zone was parameterized by blocks with dimensions of



15252027, 2008, 10, Downloaded from https://agupubs.onlinelibrary.wiley.com/doi/10.1029/2008GC002040 by Cochrane Costa Rica, Wiley Online Library on [21/07/2025]. See the Terms and Conditions (https://onlinelibrary.wiley.com/terms-and-conditions) on Wiley Online Library for rules of use; OA articles are governed by the applicable Creative Commons License

100 km along strike, 20 km across strike, and 20 km in depth (Figure 4), except for the topmost layer, in which blocks were 500 m in depth and 10 km in both horizontal directions. The smaller block size in the uppermost layer partly accounts for near surface effects. Smoothing constraints between blocks were not imposed, since our results do not exhibit short-wavelength fluctuations between blocks.

[28] The optimal block parameterization for resolving three-dimensional structure was determined by testing the case where the along-arc blocks were split in half (50 km wide) and also the case where the across-arc block widths were doubled (40 km wide). When blocks are smaller than preferred dimensions, resolution is decreased within the wedge. When blocks are bigger than those of the preferred parameterization, smaller-scale structure is averaged out without improving formal resolution.

[29] Unconstrained inversions (unrealistic negative $Q_S^{-1}$ values allowed) as well as inversions that constrain attenuation to be positive were performed. For the constrained case, iterations were performed in which negative $Q_S^{-1}$ values were replaced by small positive start model values with increased damping.

## 3. Results

[30] Attenuation profiles beneath the dense station lines in Nicaragua and Costa Rica manifest large variations in $S$ and $P$ attenuation from the slab to wedge (Figures 5a–5h), while variations in bulk attenuation are more muted (Figures 5i–5j).

### 3.1. Bulk Attenuation Results

[31] Although the results of the joint inversions for shear and bulk attenuation imply some bulk attenuation (Figures 5i–5j), we conducted a series of tests to evaluate the magnitude of bulk attenuation that is required by the data. Shear attenuation most likely dominates in the upper mantle [*Karato and Spetzler*, 1990]. Indeed, in these inversions $P$ wave attenuation, which includes the effects of shear and bulk attenuation, broadly resembles $S$ wave attenuation (Figure 5). $Q_P/Q_S$ values are on the order of 1, reaching as high as 1.4 and 1.8 in the most attenuating zones beneath Nicaragua and Costa Rica, respectively.

[32] To consider the resolvability of bulk attenuation, several tests were performed on the separate inversions of $P$ wave t* values for $P$ wave attenuation (Figures 5a–5b) and $S$ wave t* values for $S$ wave attenuation (Figures 5c–5d). Bulk attenuation was calculated from $P$ and $S$ wave attenuation models assuming various $V_P/V_S$ ratios (1.7–1.9) [*Stachnik et al.*, 2004]. Bulk attenuation amplitudes were small, 20% or less than those of shear attenuation in the well-resolved region of the mantle wedge. In another test, $P$ wave attenuation was converted to shear wave attenuation, assuming that bulk attenuation was nonexistent. The resulting model was very similar to the shear attenuation obtained directly from the $t_s^*$ measurements, generally within 10% of the original model in all well-resolved portions of the mantle wedge. Again, significant bulk attenuation was not required.

[33] In another type of test, joint inversions of $t_P^*$ and $t_S^*$ data were performed for $Q_S^{-1}$ assuming that bulk attenuation was nonexistent, and then the residual of the $P$ data was inverted for a conservative estimate of $Q_\kappa^{-1}$. Note that this last test required the mean residual for the $P$ wave data to be greater than zero after the initial inversion for $Q_S^{-1}$, which is what was observed. However, while a nonzero, positive mean residual for $P$ wave data could be indicative of the need for bulk attenuation in the mantle, it could also be caused by shallow $P$ wave attenuation owing to scattering. It has been shown that the frequency dependence of $P$ wave attenuation can be as great or greater than that of $S$ wave attenuation in the crust, and similarly, $P$ wave attenuation itself may be equal to or greater than that of $S$ wave attenuation in the upper plate [e.g., *Schlotterbeck and Abers*, 2001]. Bulk attenuation structure and amplitudes from this test were very similar to that of the joint inversion (Figures 5i–5j). Regardless, the mantle wedge bulk attenuation that results from the previously described test was generally less than 50% of the magnitude of the shear attenuation in the mantle wedge, and either small or negligible (in general $Q_\kappa \geq 200$) in all well-resolved regions of the mantle wedge.

[34] In addition to the joint inversion that allowed bulk attenuation in both the crust and the mantle (Figures 5i–5j), inversions were performed that constrained bulk attenuation to be only in the crust or only in the mantle, by increasing the a priori model uncertainty to $Q_\kappa^{-1} = 0.001667$ in respective layers, thereby decreasing the effective damping. In a third case, bulk attenuation was allowed in a shallow surface layer (up to 500 m) and damped to negligible values at greater depths ($Q_\kappa^{-1}$ uncertainty = 0.000333). These very different assumptions regarding bulk attenuation have little effect on the



15252027, 2008, 10, Downloaded from https://agupubs.onlinelibrary.wiley.com/doi/10.1029/2008GC002040 by Cochrane Costa Rica, Wiley Online Library on [21/07/2025]. See the Terms and Conditions (https://onlinelibrary.wiley.com/terms-and-conditions) on Wiley Online Library for rules of use; OA articles are governed by the applicable Creative Commons License

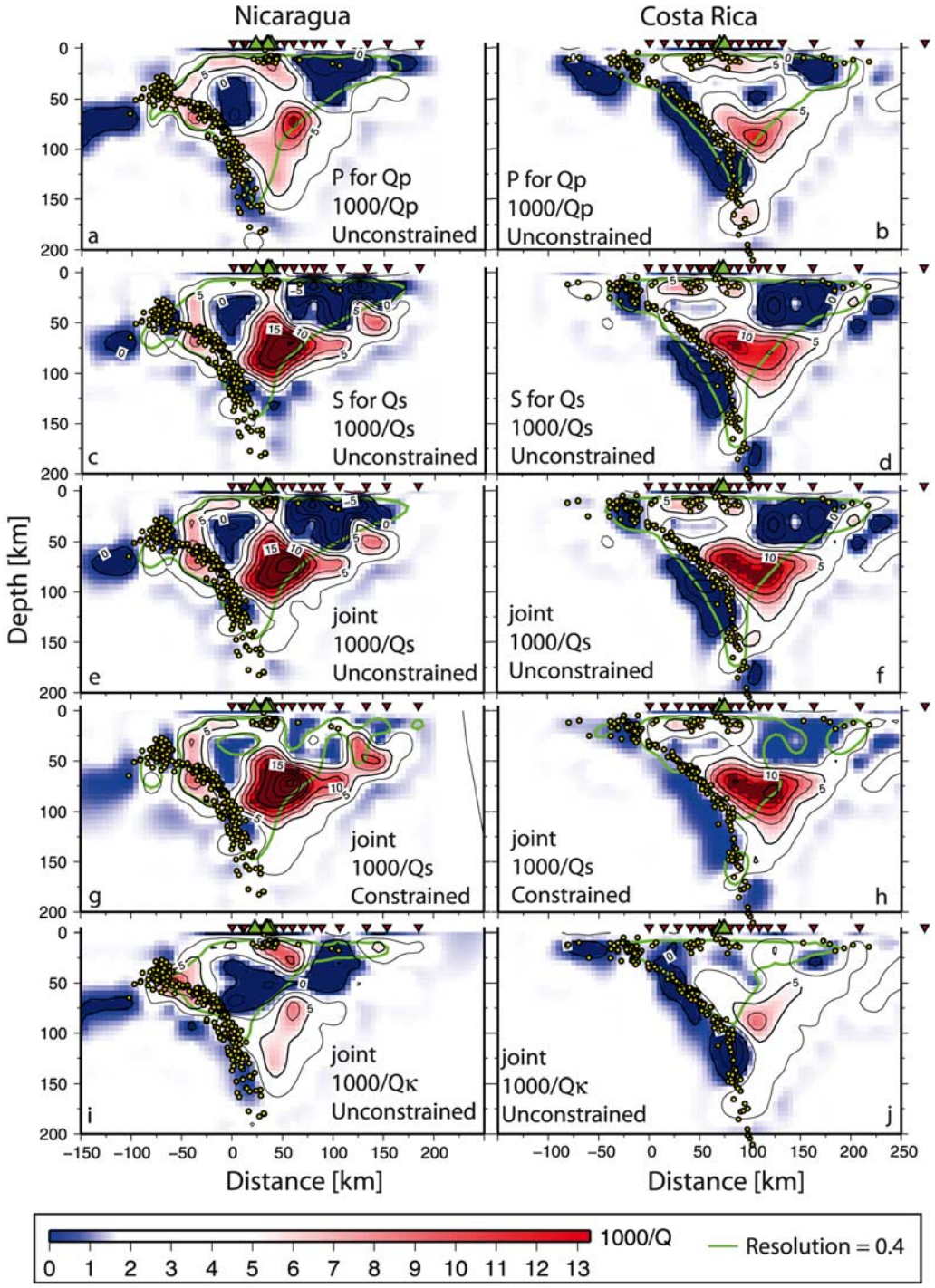


**Figure 5.** Attenuation results. Results of (a–b) unconstrained inversion of *P* wave data for *P* attenuation, (c–d) unconstrained inversion of *S* data for shear attenuation, (e–f) unconstrained joint inversion of *P* and *S* wave data for bulk and shear attenuation (shear attenuation is shown), (g–h) constrained inversion of *P* and *S* wave data for shear and bulk attenuation (shear attenuation is shown), and (i–j) unconstrained inversion of *P* and *S* wave data for shear and bulk attenuation where damping parameters permit bulk attenuation in the crust and mantle (bulk attenuation is shown). Constrained inversions enforce nonnegativity in $Q_S^{-1}$. Green line represents resolution = 0.4. Yellow circles indicate seismicity. Red inverted triangles mark station locations. Green triangles mark volcanoes. The projection width is 50 km on either side of the cross-section line.



15252027, 2008, 10, Downloaded from https://agupubs.onlinelibrary.wiley.com/doi/10.1029/2008GC002040 by Cochrane Costa Rica, Wiley Online Library on [21/07/2025]. See the Terms and Conditions (https://onlinelibrary.wiley.com/terms-and-conditions) on Wiley Online Library for rules of use; OA articles are governed by the applicable Creative Commons License

**Table 1.** Minimum $Q_S$ Results at 70 km Depth

| Inversion | Variance[a] × $10^{-3}$ | Nicaragua | | Costa Rica | |
|---|---|---|---|---|---|
| | | Joint[b] | S[c] | Joint[b] | S[c] |
| $Q_S^{-1}$ uncertainty[d] = 0.001667 | 7.472 | 44 ± 2 | 50 ± 3 | 66 ± 3 | 69 ± 3 |
| Constrained[e] | 7.688 | 39 ± 2 | 43 ± 2 | 64 ± 3 | 67 ± 3 |
| $Q_S^{-1}$ uncertainty[d] = 0.001 | 7.718 | 64 ± 4 | 73 ± 5 | 80 ± 4 | 84 ± 4 |
| $Q_S^{-1}$ uncertainty[d] = 0.0013 | 7.577 | 52 ± 3 | 60 ± 4 | 71 ± 3 | 75 ± 4 |
| $Q_S^{-1}$ uncertainty[d] = 0.0021 | 7.409 | 38 ± 2 | 44 ± 3 | 62 ± 3 | 65 ± 3 |
| $Q_S^{-1}$ start model[f,g] = 0.0013 | 7.481 | 44 ± 2 | 51 ± 3 | 66 ± 3 | 70 ± 3 |
| $Q_S^{-1}$ start model[f,g] = 0.0021 | 7.470 | 44 ± 2 | 50 ± 3 | 66 ± 3 | 69 ± 3 |
| Frequency independent[f] | — | 66 ± 5 | 71 ± 6 | 102 ± 8 | 103 ± 8 |
| Include negative $t^*$[f] | — | 41 ± 2 | 47 ± 2 | 77 ± 4 | 81 ± 4 |
| $Q_\kappa^{-1}$ allowed in crust[f,h] | 7.422 | 44 ± 2 | — | 66 ± 3 | — |
| $Q_\kappa^{-1}$ allowed in crust and mantle[f,h] | 7.325 | 45 ± 2 | — | 68 ± 3 | — |

[a] Reported variances correspond to shear attenuation model at depths greater than 500 m.
[b] Joint columns correspond to inversions of $t_S^*$ and of $t_P^*$ for $Q_S^{-1}$ and $Q_\kappa^{-1}$.
[c] S columns correspond to straight inversions of $t_S^*$ for $Q_S^{-1}$.
[d] Uncertainties correspond to a priori parameters that are inversely related to damping.
[e] The preferred model is the constrained model. All other values in table correspond to unconstrained inversions for comparison.
[f] $Q_S^{-1}$ uncertainty equals 0.001667.
[g] $Q_S^{-1}$ start model in all other rows equals 0.001667.
[h] $Q_\kappa^{-1}$ uncertainty increased to 0.001667 in respective layers. In all inversions except the bottom two ($Q_\kappa^{-1}$ allowed in crust and $Q_\kappa^{-1}$ allowed in crust and mantle), bulk attenuation is damped to 0 in all model layers deeper than 500 m.

magnitude of shear attenuation in the joint inversions, within our formal error bars (Table 1), and the related changes in data misfit (variance values in Table 1) are not large. Furthermore, in all inversions the magnitude of bulk attenuation in the area of high resolution is generally less than that of shear attenuation, except for some parts of the downgoing slab and upper plate (Figures 5i–5j) where bulk and shear magnitudes are comparable.

[35] To summarize, the general pattern of *P* wave attenuation is consistent with that observed in the shear attenuation. When allowed, bulk attenuation is generally muted in magnitude compared to shear attenuation in the well-resolved portions of the mantle wedge. Bulk attenuation is not robustly constrained in the sense that allowing it in the crust and/or mantle does not dramatically reduce data misfit. Nor do very different assumptions regarding bulk attenuation have significant impact on shear attenuation structure. Shear attenuation dominates the inversion results. Therefore, shear attenuation results are the focus of this paper. Unless otherwise specified, models are shown for the cases where bulk attenuation is damped to nonexistence ($Q_\kappa^{-1}$ uncertainty = 0.000333) in the crust and the mantle at depths greater than 500 m.

## 3.2. Shear Attenuation Results: General Characteristics

[36] We present both the result of inverting $t_S^*$ for $Q_S^{-1}$ (Figures 5c–5d), and the joint inversion of $t_p^*$ and $t_S^*$ for $Q_S^{-1}$ and $Q_\kappa^{-1}$ (Figures 5e–5j). In the case of the joint inversion, both the unconstrained (unrealistic negative $Q_S^{-1}$ values allowed) (Figures 5c–5f) and the constrained case (positive $Q_S^{-1}$ values enforced) (Figures 5g–5h) are shown. The patterns of attenuation in all three sets of models are the same, and the maximum amplitudes of attenuation and their locations (in the wedge) are very similar among models (Table 1). The constrained joint inversion is the preferred result given that it represents both *P* and *S* data sets, and since positive attenuation is more physically realistic. The results of the constrained joint inversion are also presented in map view (Figure 6) to demonstrate the continuity of our results and aid visualization of attenuation variations between Costa Rica and Nicaragua.

[37] High shear attenuation ($Q_S < 200$) is imaged in the subarc wedge with low shear attenuation ($Q_S > 600$) in most parts of the slab and the back-arc side of the upper plate beneath both Costa Rica and Nicaragua (Figures 5c–5h). In addition, a low-to-moderate shear attenuation zone ($Q_S > 200$) in the tip of the wedge corner is observed.

[38] There are first-order differences in the attenuation structures of the mantle wedges beneath Nicaragua and Costa Rica. A larger zone of greater shear attenuation characterizes the wedge beneath Nicaragua. Beneath the volcanic arc, where resolution is good ($R > 0.4$), the zone of highest shear attenuation ($Q_S < 100$) in Nicaragua spans >50 km



15252027, 2008, 10, Downloaded from https://agupubs.onlinelibrary.wiley.com/doi/10.1029/2008GC002040 by Cochrane Costa Rica, Wiley Online Library on [21/07/2025]. See the Terms and Conditions (https://onlinelibrary.wiley.com/terms-and-conditions) on Wiley Online Library for rules of use; OA articles are governed by the applicable Creative Commons License

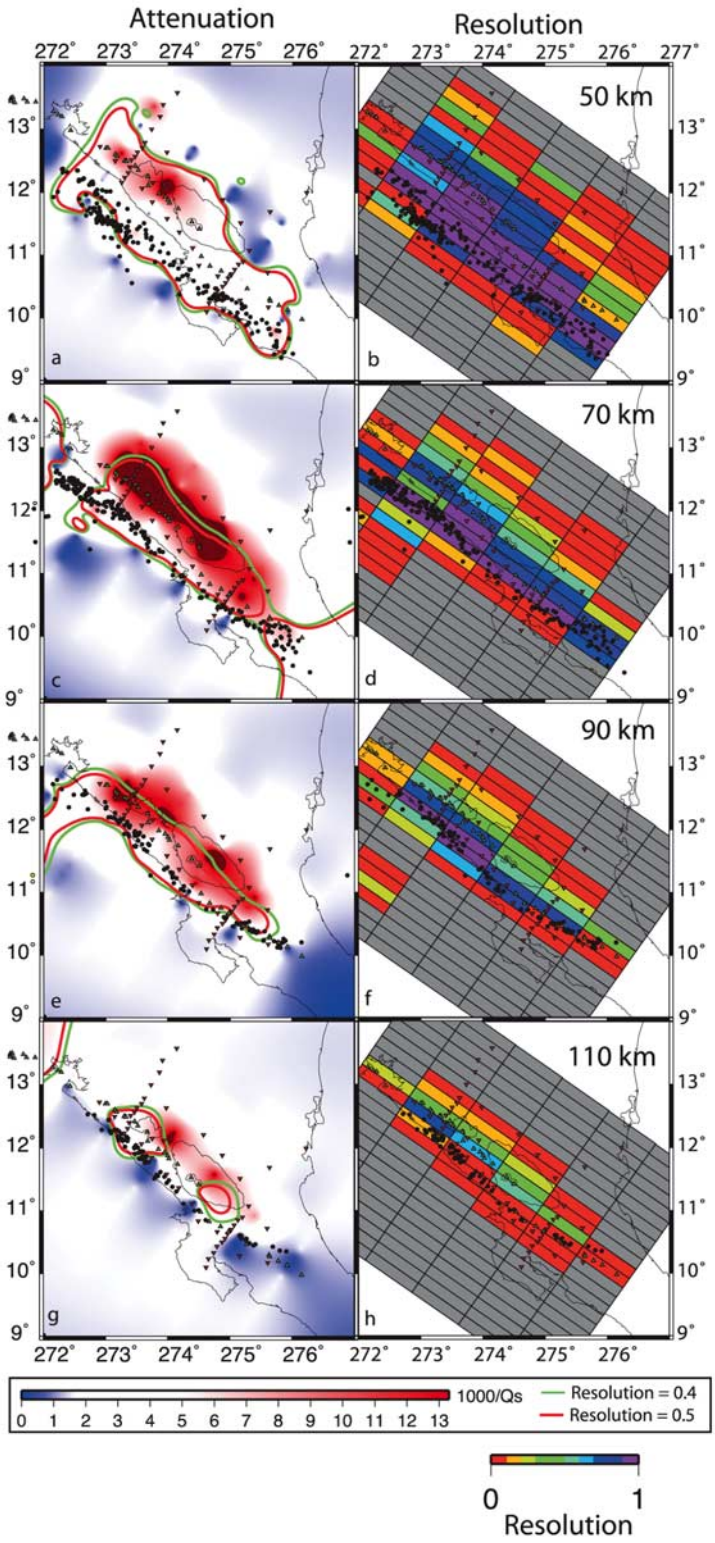


**Figure 6.** Shear attenuation results, map view. We present a map view of the constrained $Q_S$ results from the joint inversion (a, c, e, g) at 50, 70, 90, and 110 km depth, respectively (the depth midpoints of the block parameterization) and (b, d, f, h) the corresponding resolution matrix values. Yellow circles indicate seismicity. Green line represents resolution equal to 0.4. Red line represents resolution equal to 0.5. Red triangles indicate station locations. Green triangles indicate volcanoes. Black lines outline the coast.



15252027, 2008, 10, Downloaded from https://agupubs.onlinelibrary.wiley.com/doi/10.1029/2008GC002040 by Cochrane Costa Rica, Wiley Online Library on [21/07/2025]. See the Terms and Conditions (https://onlinelibrary.wiley.com/terms-and-conditions) on Wiley Online Library for rules of use; OA articles are governed by the applicable Creative Commons License

in depth versus <25 km in Costa Rica. The depth extent of the zone of highest attenuation is also greater directly beneath the arc of Nicaragua (~45–105 km depth) versus Costa Rica (~60–85 km depth). The zone of high resolution extends to comparable depths beneath the two countries (~150 km), indicating that the observed difference in the depth of the high attenuation anomaly is real. The magnitude of greatest shear attenuation reached throughout the wedge in the preferred model, the constrained joint inversion, is also higher beneath Nicaragua ($Q_S$ = 39) than that beneath Costa Rica ($Q_S$ = 64) (Table 1). A more continuous view of the along-arc variation in maximum wedge attenuation can be seen in the map view through the model at a depth of 70 km (Figure 6). Wedge attenuation remains higher in Nicaragua just to the southeast of the point where the arc makes its right-lateral step. This zonation correlates laterally with the arc-parallel extent of a slow *P* wave velocity layer within the subducting slab that has been interpreted as anomalously hydrated crust and mantle [*Syracuse et al.*, 2008].

[39] The upper plate in both countries is characterized by low shear attenuation. Beneath Costa Rica the upper plate is a continuous region where $Q_S$ > 600 (Figures 5f and 5h). Beneath Nicaragua this region varies between moderate and low shear attenuation (200 < $Q_S$ < 600) in the constrained inversion (Figure 5g) but retains a coherent large low-attenuation (negative) zone in the unconstrained case (Figure 5e).

[40] The slabs of Costa Rica and Nicaragua also have different shear attenuation characters (Figures 5c–5h). The majority of the slab beneath Costa Rica exhibits low shear attenuation, $Q_S$ > 600, while the slab beneath Nicaragua is moderately attenuating, $Q_S \sim 400$. There are more paths through the Costa Rican slab than through the Nicaraguan slab since the Costa Rican seismic line extends further past the corner of the wedge onto the Nicoya Peninsula; in Nicaragua, such station locations would be offshore. However, both checkerboard and real structure recovery tests indicate that resolution in the slabs beneath the two countries is comparable, and therefore the majority of the observed difference between the slabs of Nicaragua and Costa Rica is real (see section 4.1). There is also a region of the slab that has higher attenuation relative to the rest of the slab ($Q_S$ < 200) at 50–75 km beneath Nicaragua and ($Q_S$ < 600) at 25–50 km beneath Costa Rica. This feature is toward the edge of good resolution; however, checkerboard testing indicates that such a feature should be resolvable.

[41] A zone of particularly low shear attenuation in the corner of the wedge beneath Nicaragua ($Q_S$ > 600) is imaged, the largest anomaly existing at 20–40 km depth. Beneath Costa Rica the wedge corner is also less attenuating than the subarc wedge. However, the corner beneath Costa Rica exhibits moderate shear attenuation, 400 < $Q_S$ < 800.

## 3.3. Shear Attenuation Results: Maximum Amplitude

[42] The magnitudes of the attenuation results are somewhat dependent on damping. To test the range of attenuation amplitude in the wedge, assuming standard block dimensions (20 km × 20 km in the arc-normal direction and as shown in Figure 4), a range of damping parameters corresponding to models with moderate variances and model lengths were employed (Figure 7 and Table 1). For these models the formal $Q_S^{-1}$ uncertainty ranged from 0.001 to 0.0021. The corresponding ranges of maximum attenuation are $Q_S$ = 38–64 and $Q_S$ = 62–80 beneath Nicaragua and Costa Rica, respectively. These values correspond to unconstrained joint inversion results in single blocks at 70 km depth beneath each country that are consistently the most attenuating locations. Although the constrained joint inversions are the preferred results, the effects of variable damping may be more directly compared in the unconstrained inversions. Both the variance and model length of the constrained joint inversion fall within the accepted range (Figure 7 and Table 1). Also, the amplitudes of straight inversions of $t_S^*$ for $Q_S^{-1}$ are very similar to the preferred joint results (Table 1), and if the two sets of inversions, straight and joint, are used together to define a range of acceptable inverse attenuation, it is only slightly broader: $Q_S$ = 38–73 and $Q_S$ = 62–84 beneath Nicaragua and Costa Rica, respectively.

## 3.4. Shear Attenuation Results: Minimum Parameter Models

[43] Given the variations of maximum wedge attenuation with damping in the standard model parameterizations, we also constructed models in which wedge blocks were large enough to yield attenuation values that were more independent of damping and more uniquely resolved. In these latter models, single parameters represent the upper plate, the high-attenuation mantle wedge (one or two zones),



15252027, 2008, 10, Downloaded from https://agupubs.onlinelibrary.wiley.com/doi/10.1029/2008GC002040 by Cochrane Costa Rica, Wiley Online Library on [21/07/2025]. See the Terms and Conditions (https://onlinelibrary.wiley.com/terms-and-conditions) on Wiley Online Library for rules of use; OA articles are governed by the applicable Creative Commons License

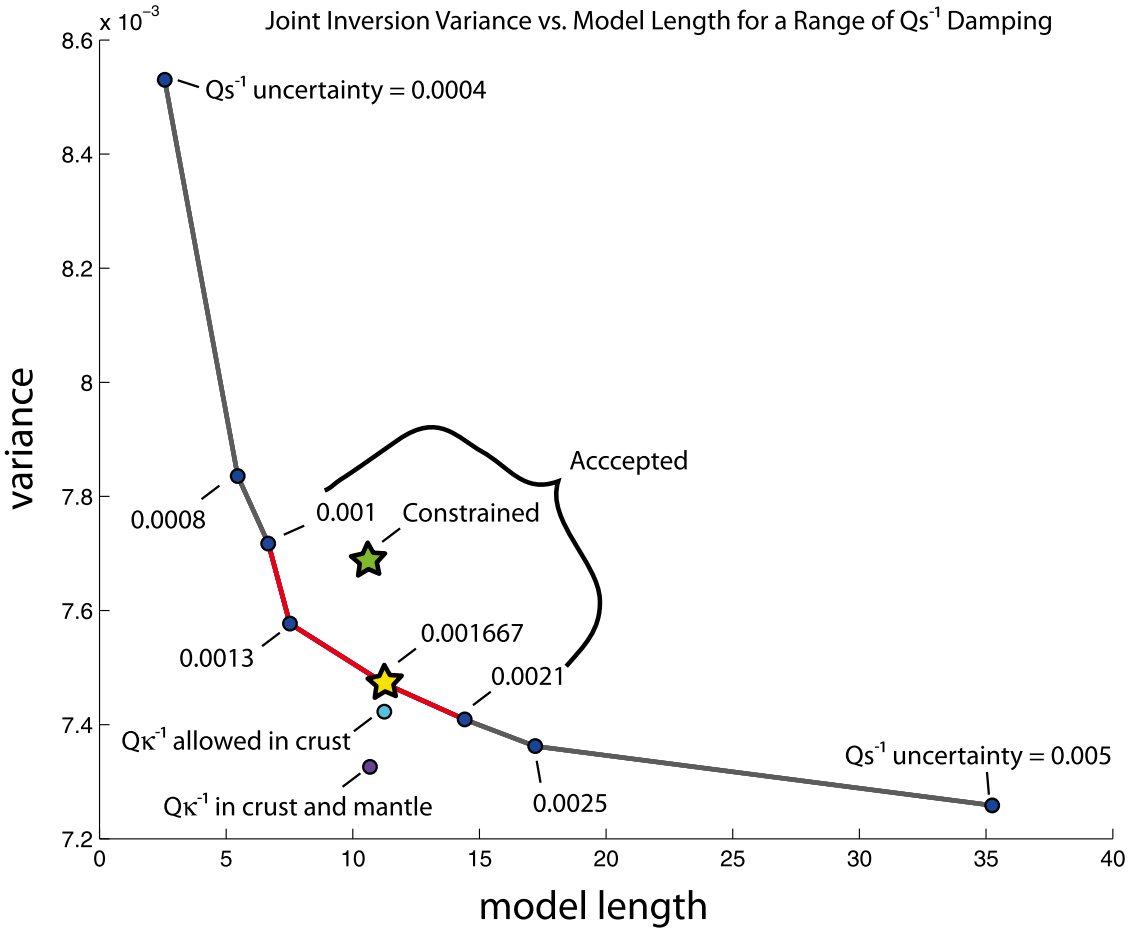


**Figure 7.** Tomographic variance versus model length. The variances of joint tomographic $Q_S^{-1}$ models at depths greater than 500 m are compared to corresponding model lengths for a range of damping parameters. Damping on $Q_S^{-1}$ decreases along the gray line as model length increases and variance decreases. The blue points connected by the red line represent the range of $Q_S^{-1}$ uncertainty (0.001–0.0021) used to define the range of attenuation amplitude. The yellow star represents the unconstrained model in which uncertainty in $Q_S^{-1}$ is 0.001667 (Figures 5e–5f), and the green star represents the constrained case (Figures 5g–5h). The cyan and purple circles off the red and gray line represent the cases where bulk attenuation is allowed in the crust (not shown) and the crust and mantle (Figures 5i–5j), respectively.

slab, and the mantle surrounding the high-attenuation wedge (Figure 8).

[44] Average wedge inverse attenuation values (combined red and pink zone in Figure 8) are $Q_S$ = 76–78 beneath Nicaragua and $Q_S$ = 84–88 beneath Costa Rica for the same range of $Q_S^{-1}$ damping described in section 3.3 (Table 2). Inversions were also performed in which the high-attenuation wedge is divided into two zones, one directly beneath the arc (pink zone in Figure 8), and one on the back-arc side of the wedge (red zone in Figure 8). The most attenuating zone beneath Nicaragua is on the back-arc side of the wedge, $Q_S$ = 65–73 (back arc) versus $Q_S$ = 81–82 (arc). The two sides are more comparable in Costa Rica: $Q_S$ = 83–87 (arc) versus $Q_S$ = 87–99 (back arc). The results from these inversions provide strong evidence that the mantle wedge beneath Nicaragua is more attenuating than that beneath Costa Rica, outside the range of formal error and error from damping parameters.

[45] The minimum parameter inversions are more stable, i.e., less variation in $Q_S^{-1}$ amplitude with respect to damping, in comparison to inversions with the standard parameterization. The minimum parameter models are better resolved, with resolution matrix diagonals that vary from 0.8353 to 0.9995, and $Q_S^{-1}$ is therefore more reliable. However, the larger block sizes in these parameterizations may also average small-scale attenuation variations, and greater attenuation may exist in the wedge than can be imaged using this type of



15252027, 2008, 10, Downloaded from https://agupubs.onlinelibrary.wiley.com/doi/10.1029/2008GC002040 by Cochrane Costa Rica, Wiley Online Library on [21/07/2025]. See the Terms and Conditions (https://onlinelibrary.wiley.com/terms-and-conditions) on Wiley Online Library for rules of use; OA articles are governed by the applicable Creative Commons License

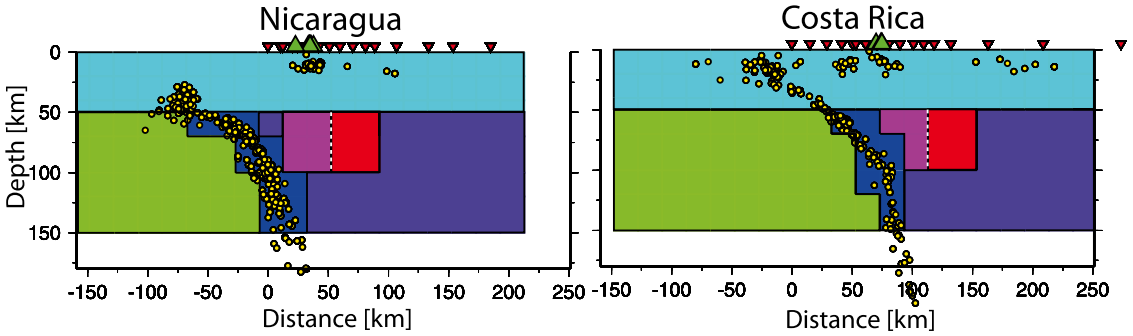


**Figure 8.** Minimum parameterization. Here the minimum parameterization blocks are shown. The parameters are as follows: the upper plate (cyan), slab (blue), high attenuation wedge (pink and red), remainder of the mantle wedge (purple), and subslab mantle (green). The slab and mantle wedges are also broken up along strike, so that variations between Nicaragua and Costa Rica may be tracked. Inversions are also performed in which the subarc mantle wedge (pink and left of the dashed line) and the back-arc side of the mantle wedge (red and right of the dashed line) are separated into two parameters to test for smaller-scale variation within the wedge. Green triangles represent volcanoes. Red triangles represent station locations. Yellow circles represent earthquakes.

model. The maximum absolute value for $Q_S$ determined by this method is somewhat larger than in the high-resolution tomography, presumably because larger volumes are averaged.

[46] Since our results assume frequency dependence ($\alpha$ = 0.27), and several former studies assume frequency independence, $t_S^*$ and $t_p^*$ were also inverted assuming frequency independence ($\alpha$ = 0) for comparison, and minimum parameterization inversions of these $t^*$ values were performed for shear and bulk attenuation structure. For this frequency-independent case, average wedge inverse attenuation values are $Q_S$ = 120–123 beneath Nicaragua and $Q_S$ = 157–164 beneath Costa Rica (Table 2). The frequency-dependent results are calculated for 1 Hz, but frequency-independent results are most sensitive to attenuation at the upper portion of the frequency band sampled [*Stachnik et al.*, 2004], approximately 7 Hz in our data for paths sampling the wedge. This range was determined by considering histogram representations of the frequency windows used in the $t^*$ inversions. The frequency-independent results are consistent with the frequency-dependent results (see section 5).

## 4. Model Assessment

### 4.1. Amplitude Recovery Tests

[47] The ability to resolve attenuation anomalies was tested with synthetic $t^*$ values from checkerboard input models (Figure 9). Checkerboards consisted of both 40 km (Figures 9a–9d) and 20 km (Figures 9e–9h) wide alternating positive and negative attenuation anomalies, $Q_S$ = 100 and $Q_S$ = 1100, separated by $Q_S$ = 600 (background), and $Q_\kappa$ = 400 and $Q_\kappa$ = 800, separated by $Q_\kappa$ = 600. Anomaly shapes and amplitudes are well retrieved in the mantle wedge between the slab and the arc for both 20 and 40 km wide anomalies, and retrieval is comparable beneath the two countries. The best recovery is in the slab, upper plate, and mantle wedge from 0 to 80 km depth from the fore

**Table 2.** Average Wedge $Q_S$ Results, Minimum Parameterization

| Area of Wedge | Nicaragua | | | | Costa Rica | | | |
|---|---|---|---|---|---|---|---|---|
| | Wedge[b] | Arc[b] | Back Arc[b] | Wedge, fi[a,b] | Wedge[b] | Arc[b] | Back Arc[b] | Wedge, fi[a,b] |
| $Q_S^{-1}$ uncertainty[c] = 0.001667 | 76 ± 1 | 81 ± 1 | 66 ± 2 | 120 ± 2 | 85 ± 2 | 84 ± 2 | 89 ± 4 | 158 ± 7 |
| $Q_S^{-1}$ uncertainty[c] = 0.001 | 78 ± 1 | 82 ± 1 | 73 ± 2 | 123 ± 3 | 88 ± 2 | 87 ± 2 | 99 ± 4 | 164 ± 7 |
| $Q_S^{-1}$ uncertainty[c] = 0.0013 | 77 ± 1 | 81 ± 1 | 69 ± 2 | 121 ± 2 | 86 ± 2 | 85 ± 2 | 93 ± 4 | 160 ± 7 |
| $Q_S^{-1}$ uncertainty[c] = 0.0021 | 76 ± 1 | 81 ± 1 | 65 ± 2 | 120 ± 2 | 84 ± 2 | 83 ± 2 | 87 ± 4 | 157 ± 7 |

[a] Here fi is frequency independent.
[b] Wedge, arc, and back arc columns correspond to zones in Figure 8 colored pink and red, pink, and red, respectively.
[c] Uncertainties correspond to a priori parameters that are inversely related to damping.



15252027, 2008, 10, Downloaded from https://agupubs.onlinelibrary.wiley.com/doi/10.1029/2008GC002040 by Cochrane Costa Rica, Wiley Online Library on [21/07/2025]. See the Terms and Conditions (https://onlinelibrary.wiley.com/terms-and-conditions) on Wiley Online Library for rules of use; OA articles are governed by the applicable Creative Commons License

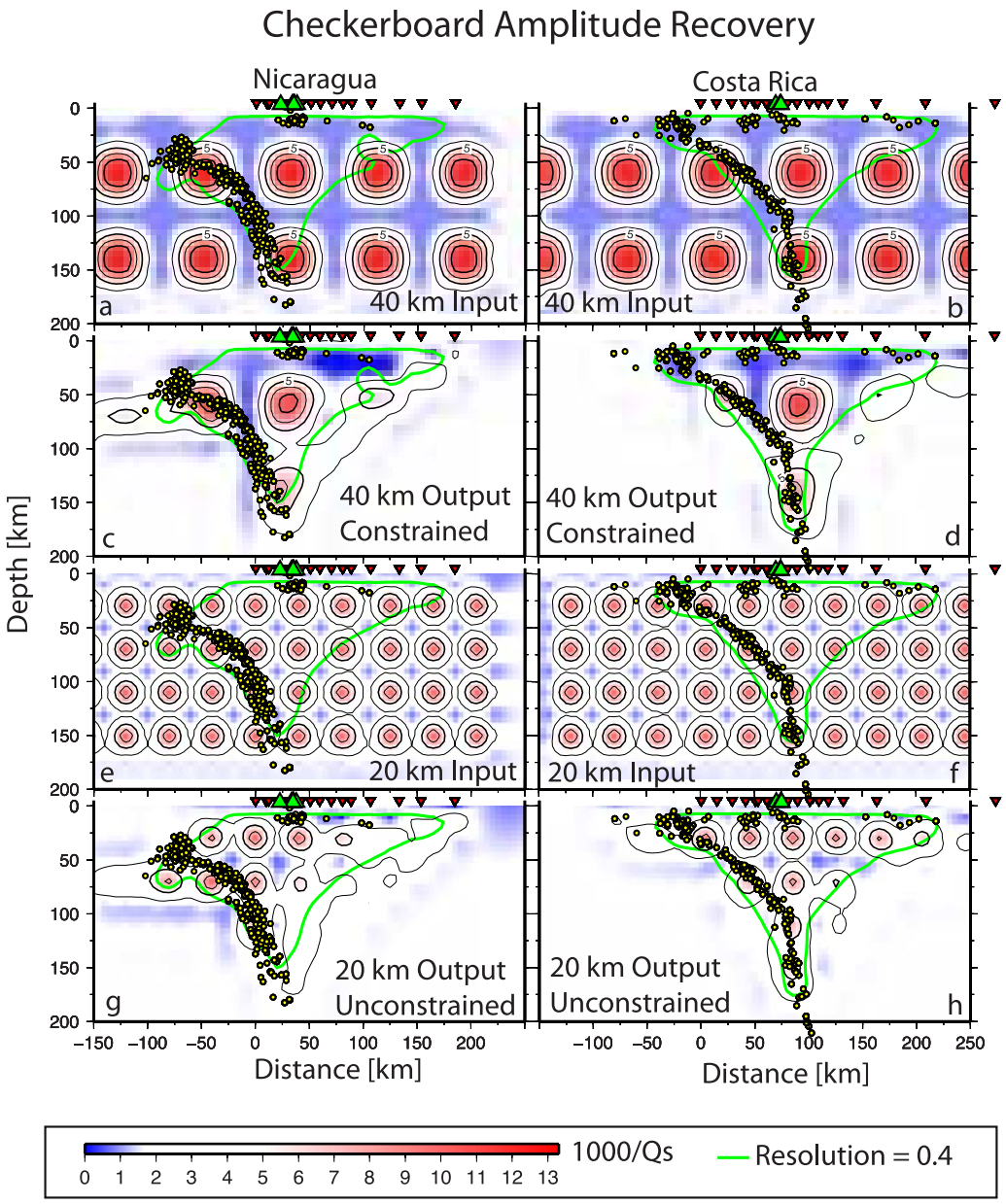


**Figure 9.** Checkerboard test. (a, b, e, f) Input and (c, d, g, h) output of checkerboard tests in Nicaragua (Figures 9a, 9c, 9e, and 9g) and Costa Rica (Figures 9b, 9d, 9f, and 9h) are presented. The green resolution contour corresponds to that from unconstrained inversion and is drawn to aid comparisons. The checkerboard in Figures 9a–9d consists of anomalies 40 km across-arc, 100 km along-arc, and 40 km in depth. The checkerboard in Figures 9e–9h consists of anomalies 20 km across-arc, 100 km along-arc, and 20 km in depth. The input inverse attenuation values of the anomalies are $Qs$ = 100 and $Qs$ = 1100, separated by blocks where $Qs$ = 600. Red inverted triangles indicate stations. Green triangles indicate volcanoes. Yellow circles indicate earthquakes. The projection width is 50 km on either side of the cross-section lines.

arc to the arc. Amplitude recovery rapidly diminishes toward the back arc and behind the slab. In the zone where resolution matrix diagonals exceed 0.4, at least 50% of original amplitudes are recovered for 20 km wide high attenuation anomalies. The larger, 40 km wide high-attenuation anomalies at 40–80 km depth beneath the arc are very well recovered (73–96% beneath Nicaragua and 82–96% beneath Costa Rica), and these anomalies are also reasonably well-resolved at deeper depths, 120–140 km beneath the arc (79% and 73% beneath Nicaragua and Costa Rica, respectively) where resolution matrix diagonal exceed 0.4.



15252027, 2008, 10, Downloaded from https://agupubs.onlinelibrary.wiley.com/doi/10.1029/2008GC002040 by Cochrane Costa Rica, Wiley Online Library on [21/07/2025]. See the Terms and Conditions (https://onlinelibrary.wiley.com/terms-and-conditions) on Wiley Online Library for rules of use; OA articles are governed by the applicable Creative Commons License

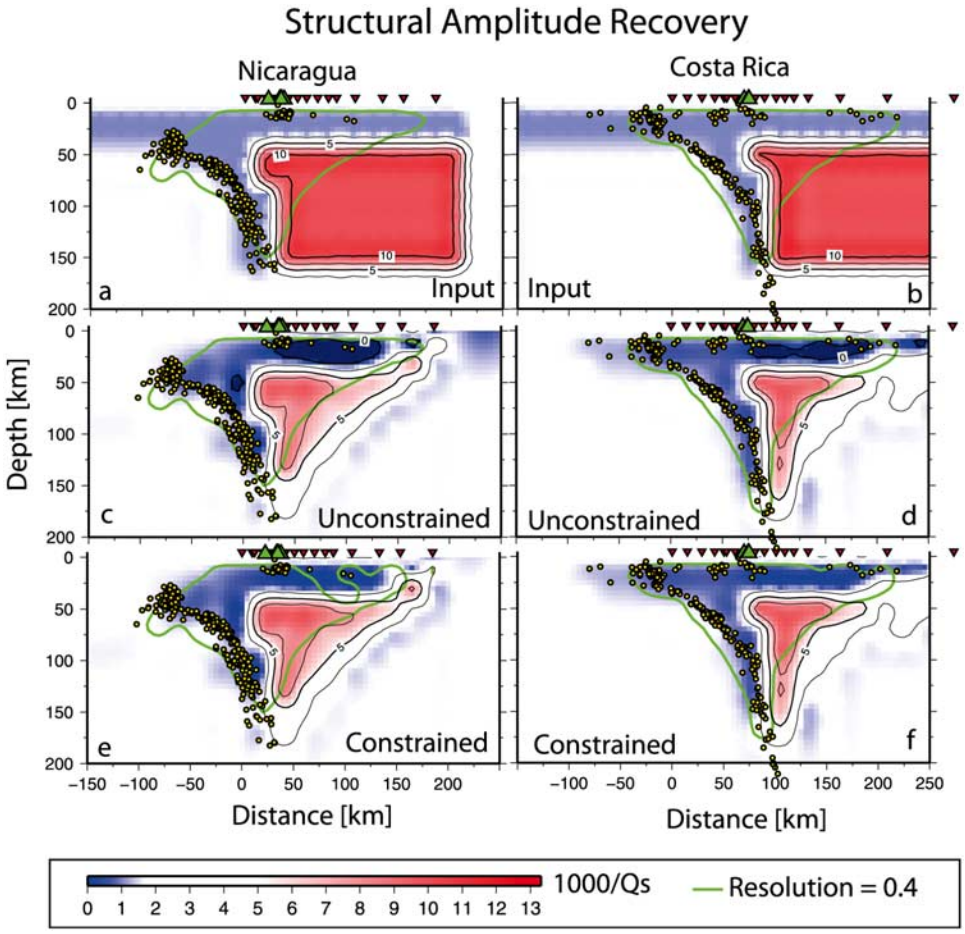


**Figure 10.** Amplitude recovery test. The (a–b) input and (c–f) output of recovery tests in Nicaragua (Figures 10a, 10c, and 10e) and Costa Rica (Figures 10b, 10d, and 10f) is presented for both the unconstrained (Figures 10c and 10d) and constrained (Figures 10e and 10f) cases. The green resolution contour is from the unconstrained inversion, and it is drawn to aid in comparisons. The same 20 × 20 × 100 km block parameterization used for the straight and joint inversions is employed here. The input values for blocks in the slab and upper plate are $Qs$ = 1000. Those in the mantle wedge are $Qs$ = 100. The input for the remainder of the blocks is the reference value, $Qs$ = 600. Red inverted triangles indicate stations. Green triangles indicate volcanoes. Yellow circles indicate earthquakes. The projection width is 50 km on either side of the cross-section lines.

[48] The ability to recover the amplitudes of anomalies corresponding to structures of interest, i.e., the slab, wedge, and upper plate (Figure 10), was also tested. This case is particularly useful for determining whether the along-arc variations apparent in the models from the real data are required. The input model was a slab, a 40 km thick upper plate ($Q_S$ = 1000), and a wedge ($Q_S$ = 100) with a 1-D low bulk attenuation model ($Q_\kappa$ = 3000). The inversion was performed for both the constrained and the unconstrained cases. Anomaly dimensions and amplitudes are well retrieved in the mantle wedge between the slab and the arc, the slab, and the upper plate. For regions within the wedge where the resolution matrix diagonals are greater than 0.4, recovery in the wedge is 70–91% beneath Nicaragua and 79–94% beneath Costa Rica. Recovery of low $Q_S^{-1}$ in the wedge corner at 50 km depth was 60–61% beneath Nicaragua and 58–65% beneath Costa Rica. The upper plate and slab are comparably retrieved beneath the two countries at greater than 60%, as deep as 100 km depth in the case of the slabs. Therefore, the along-arc variations in slab and wedge structure apparent in the real data inversions are robust.

## 4.2. Uncertainties in the Tomographic Inversion

[49] The effects of various assumptions on the overall character of the tomographic inversions as well as on the amplitudes of attenuation are described here. Tests examined the effects of



15252027, 2008, 10, Downloaded from https://agupubs.onlinelibrary.wiley.com/doi/10.1029/2008GC002040 by Cochrane Costa Rica, Wiley Online Library on [21/07/2025]. See the Terms and Conditions (https://onlinelibrary.wiley.com/terms-and-conditions) on Wiley Online Library for rules of use; OA articles are governed by the applicable Creative Commons License

assumptions regarding the frequency dependence of attenuation, the exclusion of negative $t^*$ measurements and events with greater than 50% $t^*$ measurements, the velocity model used for ray tracing and the relationship of $Q_\kappa$ to $Q_S$, variation in raypaths between the two countries, damping parameters, starting models, and block parameterization (Tables 1 and 2).

[50] Tomographic results assuming frequency-independent attenuation are reported here for comparison to studies that assume frequency independence. When frequency-independent attenuation is assumed, anomaly patterns in the wedge, slab, and upper plate are similar to those assuming frequency dependence. However, the overall magnitude of attenuation in the wedge is decreased by ~35% (Tables 1 and 2). This is expected given the tradeoff between frequency dependence (equation (3)) and the shape of the spectra model used to invert for $t^*$ in equation (2).

[51] Elimination of negative $t^*$ values and events with greater that 50% negative $t^*$ values reduces the database from 1300 (12,133 event-station pairs) to 1105 events (9602 event-station pairs) and 1097 events (9136 event-station pairs) for the $P$ and $S$ databases, respectively. This is the case assumed in the attenuation models shown in this paper. If the same events are excluded from both $P$ and $S$ data, 926 (7738 event-station pairs) remain. The models obtained with this smaller set of measurements are essentially identical to those for which events were excluded separately from $P$ and $S$ measurements.

[52] Including physically unrealistic negative $t^*$ values and events with greater than 50% negative $t^*$ values, which are low quality, in the tomographic inversions has little effect on the amplitude of shear attenuation in the final results. The overall pattern of attenuation in the wedge, upper plate, and slab remains unchanged. The main difference is enhanced negative attenuation ($1000/Q_S$ as low as $-10$) in the deep parts of the slabs (depths >110 km) beneath Nicaraguan and Costa Rica. Variation in the remainder of the cross sections is small, reductions of ~15% or less in the zone of greatest attenuation. Wedge results including negative $t^*$ are well within the range of amplitudes determined by variations in damping parameters (Table 1).

[53] The velocity model used for ray tracing and also the partitioning of $P$ attenuation into its bulk and shear components was tested. Reasonable changes in the velocity model (~2%) have little effect on the overall character of attenuation. The effect on most blocks in the well-resolved regions of the mantle wedge is less than ~10%.

[54] Variations in raypaths between Nicaragua and Costa Rica do not cause artifacts in the attenuation results. It is true that the arc-perpendicular station line in Costa Rica extended further toward the trench than that in Nicaragua. Seismometer installations at these locations in Costa Rica were enabled by the existence the Nicoya peninsula (Figure 1). However, inversions were performed that excluded information from the Nicoya peninsula. Slab and upper plate attenuation remained unchanged. Maximum wedge attenuation in both countries decreased in parallel, and only slightly, by just less than 3%. Therefore, the difference in attenuation between Costa Rica and Nicaragua is robust and not an artifact of variations in raypaths.

[55] The starting model has a minimal effect on our final results. For example, increasing or decreasing the starting $Q_S^{-1}$ (0.001667) or $Q_\kappa^{-1}$ (0.00033) model by 25% has an effect on the regular variance of <2% and an effect on the amplitude of shear attenuation that is imperceptible in the cross-section figures presented here, <2% change in individual blocks. Again, results are well within the range of amplitudes determined by variations in damping parameters (Table 1).

[56] A priori $Q_S^{-1}$ uncertainty has a greater effect on the amplitude of our final results from the standard model parameterization as previously discussed (section 3.3). Decreasing $Q_S^{-1}$ uncertainty by 25% results in a variance increase of 1.4%, and a $Q_S^{-1}$ decrease of up to 20% in individual blocks in the wedge (Table 1). However, damping on bulk attenuation has less of an effect on shear attenuation. For instance increasing uncertainty in $Q_\kappa^{-1}$ by 406% to 0.001667 has the effect of a 2% reduction in $Q_S^{-1}$ variance and also a 2% reduction in $Q_S^{-1}$. In the preferred parameterization, uncertainty in amplitude corresponding to variations in $Q_S^{-1}$ damping is accounted for by choosing a range of acceptable damping and corresponding attenuation (section 3.3). In the minimum parameter models, the effects of damping on $Q_S^{-1}$ are small (Table 2).

## 5. Discussion

[57] Shear attenuation may reflect the competing effects of temperature, hydration, and melt, and separating these contributions can be challenging. While temperature [*Jackson et al.*, 2002; *Faul and Jackson*, 2005] and hydration [*Karato*, 2003; *Aizawa et al.*, 2008] correlate with attenuation,



15252027, 2008, 10, Downloaded from https://agupubs.onlinelibrary.wiley.com/doi/10.1029/2008GC002040 by Cochrane Costa Rica, Wiley Online Library on [21/07/2025]. See the Terms and Conditions (https://onlinelibrary.wiley.com/terms-and-conditions) on Wiley Online Library for rules of use; OA articles are governed by the applicable Creative Commons License

the effects of melt on shear attenuation are less certain. Recent experiments suggest that melt-facilitated grain boundary sliding may have a signature within the seismic frequency band [*Jackson et al.*, 2004]. However, if melt-squirt is the dominant mechanism its effects on shear attenuation likely lie above the frequencies we employ [*Gribb and Cooper*, 2000]. Finally, melt distributed in larger-scale structures [*Holtzman et al.*, 2003] could have an effect on shear attenuation not yet measured by experimental studies. Given this uncertainty, shear attenuation will be interpreted in terms of temperature and water, with the caveat that the contribution from melt is unknown. However, while melt effects cannot be ruled out as an explanation for portions of the observed shear attenuation pattern, the likely region of greatest melt porosity in the wedge inferred from *Vp*/*Vs* ratios [*Syracuse et al.*, 2008] is much narrower than the broad high attenuation zone observed in the wedge and does not overlap the maximum attenuation values in the standard block inversions.

[58] The inversions of $t^*$ values from the TUCAN array indicate a significantly more attenuating wedge overall beneath Nicaragua than beneath Costa Rica. Average wedge $Q_S$ values vary from 76–78 in Nicaragua to 84–88 in Costa Rica. Maximum attenuation estimates ($Q_S$ = 38–73 and 62–84) suggest that wedge attenuation may be even stronger when variations at smaller spatial scales are allowed, although uncertainties due to damping are large.

[59] The broader and stronger shear attenuation in the Nicaraguan mantle wedge correlates with trends in geochemical data. As previously described, these trends indicate greater degrees of hydration and melting and possibly greater depths of melting, beneath Nicaragua than beneath Costa Rica [*Plank and Langmuir*, 1988; 1993; *Leeman et al.*, 1994; *Reagan et al.*, 1994; *Roggensack et al.*, 1997; *Patino et al.*, 2000; *Carr et al.*, 2003; *Wade et al.*, 2006; *Benjamin et al.*, 2007; *Sadofsky et al.*, 2008].

[60] Additional insight may be gained by mapping shear attenuation to effective temperature, which includes both the effects of temperature and also volatiles if they are present [*Karato*, 2003; *Aizawa et al.*, 2008]. These calculations are mainly valid in the wedge where the effects of temperature and hydration most likely dominate the attenuation signature. Temperature values for dry conditions are calculated by scaling shear wave attenuation using parameters determined by fitting experimental results [*Faul and Jackson*, 2005], assuming a grain size (d) of 10 mm [*Evans et al.*, 2001] and an angular frequency ($\omega$) of $2\pi$, corresponding to the reference of 1 Hz. A 10 mm grain size is appropriately larger than olivine grain sizes observed in the exposed Talkeetna arc section just below the Moho (2 mm) [*Mehl et al.*, 2003] given the greater depth of the attenuation maximum in our models. A grain size of 10 mm is also greater than olivine and pyroxene grain sizes in xenoliths from Cerro Mercedes in the Costa Rican back arc (0.5–4 mm) [*Lindsay et al.*, 2006] which makes sense because the xenoliths appear to have originated from colder mantle regions than the wedge asthenosphere reflected in the attenuation values. There is some uncertainty in this value, and decreasing grain size to 3 mm has the effect of decreasing effective temperature by ~50–60°C for the attenuation ranges reported here. Minimum inverse attenuation values, $Q_S$ = 38–73 and 62–84 for Nicaragua and Costa Rica, respectively, scale to effective maximum temperature ranges of 1379–1500°C and 1356–1408°C. Average inverse attenuation values for the entire high attenuation wedge ($Q_S$ = 76–78 and $Q_S$ = 84–88 beneath Nicaragua and Costa Rica, respectively) correspond to effective temperature ranges of 1368–1372°C and 1348–1356°C. Considering the wedge halves with higher attenuation (Table 2), the temperature ranges are 1379–1399°C and 1350–1358°C, respectively.

[61] Because abundant geochemical evidence indicates that wet melting occurs in subduction zone wedges, actual wedge temperature can be calculated by adjusting (decreasing) the calculated effective temperatures for the effects of hydration [e.g., *Karato*, 2003]. To account for hydration, we make the assumption that the water contents of olivine melt inclusions in arc magmas, corrected for partitioning, represent the average hydration of olivine in the wedge region roughly beneath arc. Although along-arc transport of mantle wedge material has been proposed [e.g., *Hoernle et al.*, 2008], we are assuming that once melt is created in the wedge, it moves to the surface in the same general arc segment. As discussed in section 1, the database for water contents in magmas is as yet small, and so we take advantage of the relationship in the work of *Sadofsky et al.* [2008] between $H_2O$ and Ba/La to estimate regional averages. Ba/La has been measured extensively, and we take the volcano averages in the work of *Carr et al.* [2007] for the San Cristobal-Mombacho and Orosi-Arenal sectors of the Nicaragua and Costa Rica arcs, respectively, as they overlap with the regions



15252027, 2008, 10, Downloaded from https://agupubs.onlinelibrary.wiley.com/doi/10.1029/2008GC002040 by Cochrane Costa Rica, Wiley Online Library on [21/07/2025]. See the Terms and Conditions (https://onlinelibrary.wiley.com/terms-and-conditions) on Wiley Online Library for rules of use; OA articles are governed by the applicable Creative Commons License

represented in the Nicaragua and Costa Rica attenuation profiles. The strong decline in Ba/La from Nicaragua to Costa Rica predicts a similar decline in the $H_2O$ content of the primary magmas, from 4.9 ± 0.4 wt % to 3.3 ± 0.2 wt % $H_2O_{91}$ (which is the water concentration in magmas in equilibrium with mantle olivine of $Fo_{91}$). Because seismic response is largely governed by the behavior of olivine, the dominant mineral in the mantle, we next calculate how much water would be partitioned into olivine in equilibrium with the above melts, assuming an olivine/liquid partition coefficient of 0.0015 [*Hauri et al.*, 2006]. This predicts 74 wt ppm (or 1200 H/Si ppm molar) and 50 wt ppm (or 815 molar) for Nicaragua and Costa Rica olivine, respectively. This amount of hydration would mean that our maximum effective mantle temperature results scaled from attenuation would translate to actual temperatures ~140–160°C lower beneath Nicaragua, and ~120–130°C lower beneath Costa Rica according to equation (6) and Figure 3 in the work of *Karato* [2003], or approximately 1237–1338°C and 1236–1280°C beneath Nicaragua and Costa Rica, respectively. Average wedge temperatures scale to ~1230 ± 20°C after correcting for the effects of hydration. Average hydration-corrected temperatures for the more highly attenuating wedge halves are ~1240 ± 20°C. Overall, the different wedge attenuation values for the two regions scale to consistent temperatures once water content is corrected for, suggesting that greater hydration in the Nicaraguan wedge dominates the observed along-arc attenuation variation.

[62] The importance of wedge hydration is further underscored by comparisons with petrological modeling. Although bulk magma compositions in the vicinity of the Nicaragua and Costa Rica attenuation profiles are significantly different, they imply a similar temperature of 1265 ± 25°C at a depth comparable to the middle of the wedge (75 km) when the water content of the primary melt is taken into account in calculating olivine-liquid temperatures [*Plank et al.*, 2007]. The 1265 ± 25°C temperature agrees well with the maximum water-corrected temperatures inferred from attenuation for a grain size of 10 mm, and they are within error of the temperatures calculated for the average wedge and the more attenuating halves of the wedge. Increasing the grain size assumed for the wedge when converting attenuation to temperature would bring the seismological and petrological estimates into even closer agreement.

[63] The zone of low shear attenuation in the shallow corner of the wedge beneath the fore arc is most likely a colder region of the wedge given typical mantle isotherms [*Peacock*, 1996; *Kincaid and Sacks*, 1997; *van Keken et al.*, 2002; *Kincaid and Griffiths*, 2004; *Peacock et al.*, 2005; *Cagnioncle et al.*, 2007]. A zone of low shear attenuation in the wedge corner has been imaged in other subduction zones such as the Andes, Alaska, and Honshu [*Myers et al.*, 1998; *Takanami et al.*, 2000; *Stachnik et al.*, 2004] and also in *P* wave attenuation beneath New Zealand and the Andes [*Eberhart-Phillips and Chadwick*, 2002; *Schurr et al.*, 2003]. Beneath Nicaragua and Costa Rica, the boundary between this low-attenuation nose and the high-attenuation region found in the rest of the wedge appears to be sharp, and intersects the slab near 80 km depth, similar to other regions [*Kincaid and Sacks*, 1997; *Schurr et al.*, 2003; *Abers et al.*, 2006]. The fact that most of the corner of the Nicaraguan wedge shows much less shear attenuation than that of Costa Rica could mean that less volatiles are released in this portion of the Nicaraguan wedge than are released in the fore-arc corner of the Costa Rican wedge. In the cold wedge corner, higher hydration would likely result in serpentinization, and although the effects of hydration on attenuation in mantle materials are still uncertain, some experimental data suggest that attenuation in serpentine is large [*Kern et al.*, 1997]. In addition, serpentinization of the Costa Rican fore-arc mantle beneath the Nicoya Peninsula has been inferred from seismic velocities [*DeShon and Schwartz*, 2004; *DeShon et al.*, 2006]. The lower attenuation in the Nicaraguan wedge corner would be consistent with the notion that volatiles flux off of the Nicaraguan wedge deeper or in a more focused zone [*Patino et al.*, 2000; *Rupke et al.*, 2002; *Carr et al.*, 2003]. Somewhat higher attenuation in the shallowest part of the Nicaraguan wedge corner (25–50 km depth) may suggest an early pulse of dehydration at a depth of roughly 50 km. Alternatively, another mechanism besides volatiles, such as poroelastic effects, could be operating in the Costa Rican wedge corner [*Budiansky et al.*, 1983].

[64] The small zone of moderate shear attenuation internal to the shallow slab (45–70 km depth beneath Costa Rica and 50–80 km beneath Nicaragua) could be indicative of hydrated slab crust and serpentinized mantle [*Kern et al.*, 1997]. This feature correlates with the location of a layer of slow *P* wave velocity in the Nicaraguan slab [*Syracuse et al.*, 2008] that has been interpreted as



15252027, 2008, 10, Downloaded from https://agupubs.onlinelibrary.wiley.com/doi/10.1029/2008GC002040 by Cochrane Costa Rica, Wiley Online Library on [21/07/2025]. See the Terms and Conditions (https://onlinelibrary.wiley.com/terms-and-conditions) on Wiley Online Library for rules of use; OA articles are governed by the applicable Creative Commons License

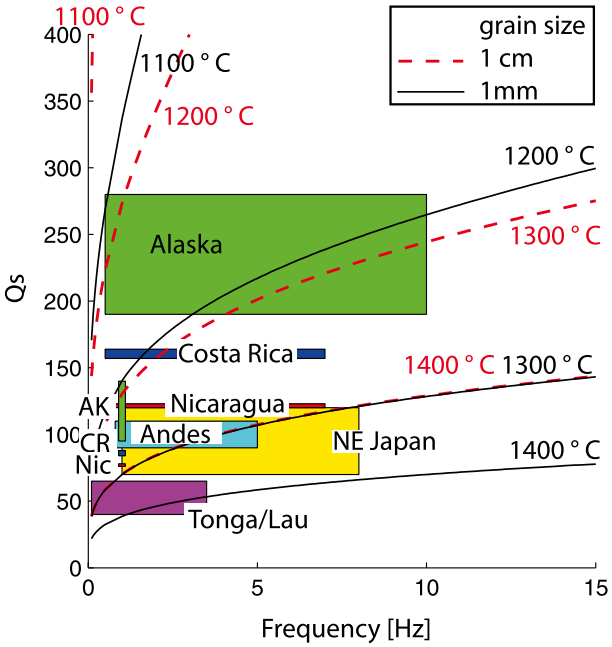


**Figure 11.** Comparison to other regions. Results for average wedge attenuation beneath Nicaragua and Costa Rica are compared to those of other shear attenuation studies. All results assuming frequency independence are represented by boxes that span the frequency bands considered by the studies. These results are most sensitive to the upper limit of the seismic frequency sampled, and that is where they should be considered for comparison to the temperature contours [*Stachnik et al.*, 2004]. Given the frequency dependence of results, comparisons between studies should also be done along the temperature contours (black and red dashed lines) from experimental results [*Faul and Jackson*, 2005]. The blue and red boxes 0.5 to 7 Hz represent the frequency-independent results for Costa Rica and Nicaragua, respectively. The results assuming frequency dependence are shown at 1 Hz (same color scheme). The figure is after *Stachnik et al.* [2004] and represents work in Alaska (green boxes) at 1 and 10 Hz [*Stachnik et al.*, 2004], the Andes (cyan box) [*Myers et al.*, 1998], Tonga Lau (magenta box) [*Roth et al.*, 1999], and Honshu (yellow box) [*Takanami et al.*, 2000]. The lines represent the model of *Faul and Jackson* [2005] for grain size equal to 1 mm (black, solid) and 10 mm (red, dashed) and pressure at 80 km depth. Note that the case where grain size is 1 mm and $T$ = 1300°C overlaps the case where grain size is 1 cm and temperature is 1400°C. Hydration would lower expected values for actual temperature in the wedge [*Karato*, 2003].

10–20% mantle serpentinization, and with a thick low-velocity waveguide layer near the slab-wedge interface [*Abers et al.*, 2003]. Slab serpentinization is supported by relatively low $\delta^{18}$O levels that are observed in Nicaraguan arc magmas and are likely related to water released from hydrothermally altered rocks in the slab, such as serpentine [*Eiler et al.*, 2005]. In addition, within the unsubducted plate updip of this arc segment, deep normal faults are observed [*Ranero et al.*, 2003], and velocities suggest 12–17% mantle serpentinization [*Ivandic et al.*, 2008]. Finally, a similar zone of relatively moderate slab shear attenuation in the shallow section of the subducted slab was also observed in Alaska [*Stachnik et al.*, 2004]. Alternatively, the presence of bulk attenuation in this zone may suggest the influence of other attenuation mechanisms than those that are thought to be in effect at the high temperatures in the wedge play a role [*Heinz et al.*, 1982; *Budiansky et al.*, 1983]. Moderate bulk attenuation in the upper plate at 0–30 km depth, extending from the arc, 50 km into the back arc, may be caused by a similar mechanism, especially beneath Nicaragua where the bulk attenuation is more pronounced. Bulk attenuation that was comparable or greater than shear attenuation was also observed in the upper plate beneath Alaska [*Stachnik et al.*, 2004].

[65] The observed attenuation structures do not uniquely identify the source of the region's prominent along-arc geochemical variations, but they do suggest some key constraints on melting processes. First, since differences in average wedge attenuation between Nicaragua and Costa Rica may be explained by the known variation in magma water content superimposed on a uniform wedge temperature field, it is reasonable to infer that volatiles released from the slab are able to permeate relatively large areas of the wedge. Second, the correlation of greater wedge attenuation in Nicaragua with the along-arc extent of the slab low-velocity zone [*Syracuse et al.*, 2008] and low $\delta^{18}$O magmatic signatures [*Eiler et al.*, 2005] suggests that along-arc differences in the amount, type, and distribution of fluids being subducted by the slab are key to wedge hydration. The apparent lack of along-arc variation in wedge temperature inferred from wedge attenuation, as well as the small along-arc variations in slab age (16 Ma to 24 Ma [*Barckhausen et al.*, 2001]), dip [*Protti et al.*, 1995; *Syracuse et al.*, 2008], and convergence rate [*DeMets*, 2001], would all tend to minimize along-arc variations in slab temperatures as a function of depth. Overall, these results therefore favor models in which the along-arc geochemical variations are controlled by input to the slab, for example models in which greater amounts of water enter the deep crust or mantle of the Nicaraguan slab mantle prior



15252027, 2008, 10, Downloaded from https://agupubs.onlinelibrary.wiley.com/doi/10.1029/2008GC002040 by Cochrane Costa Rica, Wiley Online Library on [21/07/2025]. See the Terms and Conditions (https://onlinelibrary.wiley.com/terms-and-conditions) on Wiley Online Library for rules of use; OA articles are governed by the applicable Creative Commons License

to subduction [*Rupke et al.*, 2002; *Eiler et al.*, 2005] perhaps via deeply cutting normal faults in the slab surface [*Ranero et al.*, 2003], as opposed to differences in dehydration conditions experienced by the slab.

[66] How do our attenuation models for the mantle wedge compare to models from other subduction zones? Although variable methods and scales of resolution make comparisons difficult, some first-order similarities and differences exist. The attenuation patterns in Central America are most similar to structure observed in Alaska [*Stachnik et al.*, 2004], southern Honshu [*Tsumura et al.*, 2000], and the southern Philippines [*Shito and Shibutani*, 2003] in that the zones of highest attenuation lie above the slab at depths of more than 50 km. In contrast, our attenuation patterns are quite different from those in northern Honshu [*Tsumura et al.*, 2000] and the northern Andes [*Schurr et al.*, 2003] where the zones of highest attenuation are localized at shallower, crustal depths. Tonga-Lau [*Roth et al.*, 1999] and the southern Andes [*Schurr et al.*, 2003] have strong zones of back-arc attenuation that are distinct from subarc attenuation anomalies. In Nicaragua-Costa Rica strong back-arc attenuation cannot be ruled out owing to decreased resolution far into the back arc.

[67] Average shear attenuation amplitudes from the minimum parameterization inversions are comparable to observations from other subduction zones globally (Figure 11). Given the frequency dependence of attenuation, results should be compared along effective temperature contours, and results assuming frequency independence should be considered at the high end of the sampled frequency band, i.e., the right-hand side of the colored boxes in Figure 11. For instance, note that our results assuming frequency dependence at 1 Hz are consistent with our frequency-independent results at 7 Hz in that the results lie along similar effective temperature contours. For a range of grain size assumptions (1–10 mm) our average wedge attenuation results correspond to dry effective temperatures of ~1270–1390°C and ~1250–1360°C beneath Nicaragua and Costa Rica, respectively. Taking into account the effects of water, actual wedge temperatures would be ~116–126°C and ~114–124°C less beneath Nicaragua and Costa Rica, respectively. Not correcting for water, the average magnitude of wedge attenuation beneath Nicaragua is comparable to values found for the Andes and to the low end of the range of values from Japan. Costa Rican attenuation lies in between values found for Nicaragua and Alaska.

## 6. Conclusions

[68] The mantle wedge beneath Nicaragua exhibits greater shear attenuation over a larger area than the wedge beneath Costa Rica. This result by itself implies that the Nicaraguan wedge is hotter and/or more hydrated than the Costa Rican wedge. Petrologic results indicate that water most likely dominates the observed along-arc variation in attenuation. Intermediate shear attenuation in the wedge corners of Nicaragua and Costa Rica are likely associated with colder temperatures, possibly modulated by variations in hydration/serpentinization. A zone of moderate attenuation within the slab beneath Nicaragua at shallow depths may be associated with increased water content in the crust and serpentinization in the slab mantle. Qualitatively, attenuation anomaly patterns in Central America have the closest resemblance to Alaska, southern Honshu, and southern Philippines. The magnitude of attenuation in the Nicaraguan mantle wedge is comparable to the Andes and Japan, while lower attenuation in the Costa Rican wedge lies between values for Nicaragua and Alaska.

## Acknowledgments

[69] Many people contributed to the success of the TUCAN experiment in the field, especially Pedro Perez and Allan Morales (INETER, Nicaragua), David Abt, Mariela Salas-de la Cruz and Alexis Walker (Brown University), and Laura MacKenzie and Gustavo Reyes (Boston University). Many thanks to Tim Parker and the IRIS/PASSCAL program for their expert help with the TUCAN seismometers, to Don Forsyth for his helpful comments on the manuscript, and to Nick Harmon for his coding expertise. Finally, we would like to thank Doug Wiens, Associate Editor Eli Silver, and an anonymous reviewer for thoughtful reviews. This work was supported by the National Science Foundation MARGINS Program through awards OCE-0203607 and OCE-0203650.

## References

Abercrombie, R. E. (1997), Near-surface attenuation and site effects from comparison of surface and deep borehole recordings, *Bull. Seismol. Soc. Am.*, *87*(3), 731–744.

Abers, G. A., T. A. Plank, and B. R. Hacker (2003), The wet Nicaraguan slab, *Geophys. Res. Lett.*, *30*(2), 1098, doi:10.1029/2002GL015649.

Abers, G. A., P. E. van Keken, E. A. Kneller, A. Ferris, and J. C. Stachnik (2006), The thermal structure of subduction zones constrained by seismic imaging: Implications for slab dehydration and wedge flow, *Earth Planet. Sci. Lett.*, *241*(3–4), 387–397, doi:10.1016/j.epsl.2005.11.055.



15252027, 2008, 10, Downloaded from https://agupubs.onlinelibrary.wiley.com/doi/10.1029/2008GC002040 by Cochrane Costa Rica, Wiley Online Library on [21/07/2025]. See the Terms and Conditions (https://onlinelibrary.wiley.com/terms-and-conditions) on Wiley Online Library for rules of use; OA articles are governed by the applicable Creative Commons License

Abratis, M., and G. Woerner (2001), Ridge collision, slab-window formation, and the flux of Pacific asthenosphere into the Caribbean realm, *Geology*, *29*(2), 127–130.

Aizawa, Y., A. Barnhoorn, U. H. Faul, J. D. Fitz Gerald, I. Jackson, and I. Kovács (2008), Seismic properties of Anita Bay dunite: An exploratory study of the influence of water, *J. Petrol.*, *49*(4), 841–855, doi:10.1093/petrology/egn007.

Aki, K., and P. G. Richards (1980), *Quantitative Seismology, Theory and Methods*, W. H. Freeman, San Francisco, Calif.

Anderson, D. L. (1989), *Theory of the Earth*, 366 pp., Blackwell Sci., Boston, Mass.

Anderson, J. G., and S. E. Hough (1984), A model for the shape of the Fourier amplitude spectrum of acceleration at high frequencies, *Bull. Seismol. Soc. Am.*, *74*(5), 1969–1993.

Barckhausen, U., C. R. Ranero, H. R. von Huene, S. C. Cande, and H. A. Roeser (2001), Revised tectonic boundaries in the Cocos Plate off Costa Rica: Implications for the segmentation of the convergent margin and for plate tectonic models, *J. Geophys. Res.*, *106*(B9), 19,207–19,220, doi:10.1029/2001JB000238.

Benjamin, E. R., T. Plank, J. A. Wade, K. A. Kelley, E. H. Hauri, and G. E. Alvarado (2007), High water contents in basaltic magmas from Irazu Volcano, Costa Rica, *J. Volcanol. Geotherm. Res.*, *168*(1–4), 68–92.

Brune, J. N. (1970), Tectonic stress and the spectra of seismic shear waves from earthquakes, *J. Geophys. Res.*, *75*(26), 4997–5009, doi:10.1029/JB075i026p04997.

Budiansky, B., E. E. Sumner Jr., and R. J. O'Connell (1983), Bulk thermoelastic attenuation of composite materials, *J. Geophys. Res.*, *88*(B12), 10,343–10,348, doi:10.1029/JB088iB12p10343.

Cagnioncle, A. M., E. M. Parmentier, and L. T. Elkins-Tanton (2007), The effect of solid flow above a subducting slab on water distribution and melting at convergent plate boundaries, *J. Geophys. Res.*, *112*, B09402, doi:10.1029/2007JB004934.

Carr, M. J., M. D. Feigenson, and E. A. Bennet (1990), Incompatible element and isotope evidence for tectonic control of source mixing and melt extraction along the Central American arc, *Contrib. Mineral. Petrol.*, *105*, 369–380, doi:10.1007/BF00286825.

Carr, M. J., M. D. Feigenson, L. C. Patino, and J. A. Walker (2003), Volcanism and geochemistry in Central America: Progress and problems, in *Inside the Subduction Factory, Geophys. Monogr. Ser*, vol. 138, edited by J. Eiler, pp. 153–174, AGU, Washington, D. C.

Carr, M. J., I. Saginor, and G. Alvarado (2007), Element fluxes from the volcanic front of Nicaragua and Costa Rica, *Geochem. Geophys. Geosyst.*, *8*, Q06001, doi:10.1029/2006GC001396.

Case, J. E., W. D. MacDonald, and P. J. Fox (1990), Caribbean crustal provinces; seismic and gravity evidence, in *The Caribbean Region*, *Geol. of N. Am*, vol. H, edited by G. Dengo and J. E. Case, pp. 15–36, Geol. Soc. of Am., Boulder, Colo.

Chan, L. H., W. P. Leeman, and C. F. You (1999), Lithium isotopic composition of Central American volcanic arc lavas; implications for modification of subarc mantle by slab-derived fluids, *Chem. Geol.*, *160*, 255–280, doi:10.1016/S0009-2541(99)00101-1.

DeMets, C. (2001), A new estimate for present-day Cocos-Caribbean Plate motion; implications for slip along the Central American volcanic arc, *Geophys. Res. Lett.*, *28*(21), 4043–4046, doi:10.1029/2001GL013518.

DeShon, H., and S. Schwartz (2004), Evidence for serpentinization of the forearc mantle wedge along the Nicoya Peninsula, Costa Rica, *Geophys. Res. Lett.*, *31*, L21611, doi:10.1029/2004GL021179.

DeShon, H., S. Y. Schwartz, A. V. Newman, V. González, M. Protti, L. M. Dorman, T. H. Dixon, D. E. Sampson, and E. R. Fluen (2006), Seismogenic zone structure beneath the Nicoya Peninsula, Costa Rica, from three-dimensional local earthquake P- and S-wave tomography, *Geophys. J. Int.*, *164*(1), 109–124, doi:10.1111/j.1365-246X.2005.02809.x.

Donnelly, T. W., G. S. Horne, R. C. Finch, and R. E. Lopez (1990), Northern Central America; the Maya and Chortis blocks, in *The Caribbean Region*, *Geol. of N. Am*, vol. H, edited by G. Dengo and J. E. Case, pp. 37–76, Geol. Soc. of Am., Boulder, Colo.

Eberhart-Phillips, D., and M. Chadwick (2002), Three-dimensional attenuation model of the shallow Hikurangi subduction zone in the Raukumara Peninsula, New Zealand, *J. Geophys. Res.*, *107*(B2), 2033, doi:10.1029/2000JB000046.

Eiler, J. M., M. J. Carr, M. Reagan, and E. Stolper (2005), Oxygen isotope constraints on the sources of Central American arc lavas, *Geochem. Geophys. Geosyst.*, *6*, Q06001, doi:10.1029/2006GC001396.

Escalante, G. (1990), The geology of southern Central America and western Colombia, in *The Caribbean Region*, *Geol. of N. Am*, vol. H, edited by G. Dengo and J. E. Case, pp. 201–230, Geol. Soc. of Am., Boulder, Colo.

Evans, B., J. Renner, and G. Hirth (2001), A few remarks on the kinetics of static grain growth in rocks, *Int. J. Earth Sci.*, *90*(1), 88–103.

Faul, U. H., and I. Jackson (2005), The seismological signature of temperature and grain size variations in the upper mantle, *Earth Planet. Sci. Lett.*, *234*(1–2), 119–134, doi:10.1016/j.epsl.2005.02.008.

Furukawa, Y. (1993), Magmatic processes under arcs and formation of the volcanic front, *J. Geophys. Res.*, *98*(B5), 8309–8319, doi:10.1029/93JB00350.

Gribb, T. T., and R. F. Cooper (2000), The effect of an equilibrated melt phase on the shear creep and attenuation behavior of polycrystalline olivine, *Geophys. Res. Lett.*, *27*(15), 2341–2344, doi:10.1029/2000GL011443.

Grove, T., N. Chatterjee, S. Parman, and E. Médard (2006), The influence of $H_2O$ on mantle wedge melting, *Earth Planet. Sci. Lett.*, *249*(1–2), 74–89, doi:10.1016/j.epsl.2006.06.043.

Gust, D. A., R. J. Arculus, and A. B. Kersting (1997), Aspects of magma sources and processes in the Honshu Arc, *Can. Mineral.*, *35*, 347–365.

Hauri, E. H., G. Gaetani, and T. H. Green (2006), Partitioning of water during melting of the Earth's upper mantle at H2O-undersaturated conditions, *Earth Planet. Sci. Lett.*, *248*(3–4), 715–734, doi:10.1016/j.epsl.2006.06.014.

Heinz, D., R. Jeanloz, and R. J. O'Connell (1982), Bulk attenuation in a polycrystalline Earth, *J. Geophys. Res.*, *87*(B9), 7772–7778, doi:10.1029/JB087iB09p07772.

Herrstrom, E. A., M. K. Reagan, and J. D. Morris (1995), Variations in lava composition associated with flow of asthenosphere beneath southern Central America, *Geology*, *23*(7), 617–620.

Hoernle, K., et al. (2000), Existence of complex spatial zonation in the Galapagos Plume for at least 14 m.y, *Geology*, *28*(5), 435–438, doi:10.1130/0091-7613(2000)28<435:EOCSZI>2.0.CO;2.

Hoernle, K., R. Werner, J. Phipps Morgan, D. Garbe-Schönberg, J. Bryce, and J. Mrazek (2008), Arc-parallel flow in the mantle



15252027, 2008, 10, Downloaded from https://agupubs.onlinelibrary.wiley.com/doi/10.1029/2008GC002040 by Cochrane Costa Rica, Wiley Online Library on [21/07/2025]. See the Terms and Conditions (https://onlinelibrary.wiley.com/terms-and-conditions) on Wiley Online Library for rules of use; OA articles are governed by the applicable Creative Commons License

wedge beneath Costa Rica and Nicaragua, *Nature*, *451*, 1094–1097, doi:10.1038/nature06550.

Holtzman, B. K., D. L. Kohlstedt, M. E. Zimmerman, F. Heidelbach, T. Hiraga, and J. Hustoft (2003), Melt segregation and strain partitioning; implications for seismic anisotropy and mantle flow, *Science*, *301*(5637), 1227–1230, doi:10.1126/science.1087132.

Hough, S. E., and J. G. Anderson (1988), High-frequency spectra observed at Anza, California: Implications for Q structure, *Bull. Seismol. Soc. Am.*, *78*(2), 692–707.

Ivandic, M., I. Grevemeyer, A. Berhorst, E. Flueh, and K. McIntosh (2008), Impact of bending related faulting on the seismic properties of the incoming plate offshore Nicaragua, *J. Geophys. Res.*, *113*, B05410, doi:10.1029/2007JB005291.

Iwamori, H. (1997), Heat sources and melting in subduction zones, *J. Geophys. Res.*, *102*(B7), 14,803–14,820, doi:10.1029/97JB01036.

Jackson, I., J. D. Fitz, J. D. Fitz Gerald, U. H. Faul, and B. H. Tan (2002), Grain-size-sensitive seismic wave attenuation in polycrystalline olivine, *J. Geophys. Res.*, *107*(B12), 2360, doi:10.1029/2001JB001225.

Jackson, I., U. H. Faul, J. D. Fitz Gerald, and B. H. Tan (2004), Shear wave attenuation and dispersion in melt-bearing olivine polycrystals: 1. Specimen fabrication and mechanical testing, *J. Geophys. Res.*, *109*, B06201, doi:10.1029/2003JB002406.

Karato, S. (2003), Mapping water content in the upper mantle, in *Inside the Subduction Factory*, *Geophys. Monogr. Ser*, vol. 138, edited by J. Eiler, pp. 135–152, AGU, Washington, D. C.

Karato, S., and H. A. Spetzler (1990), Defect microdynamics in minerals and solid-state mechanisms of seismic wave attenuation and velocity dispersion in the mantle, *Rev. Geophys.*, *28*(4), 399–421, doi:10.1029/RG028i004p00399.

Kelemen, P. B., J. L. Rilling, E. M. Parmentier, L. Mehl, and B. R. Hacker (2003), Thermal structure due to solid-state flow in the mantle wedge beneath arcs, in *Inside the Subduction Factory*, *Geophys. Monogr. Ser*, vol. 138, edited by J. Eiler, pp. 293–311, AGU, Washington, D. C.

Kelley, K. A., T. Plank, T. L. Grove, E. M. Stolper, S. Newman, and E. Hauri (2006), Mantle melting as a function of water content beneath back-arc basins, *J. Geophys. Res.*, *111*, B09208, doi:10.1029/2005JB003732.

Kern, H., B. Liu, and P. Till (1997), Relationship between anisotropy of P and S wave velocities and anisotropy of attenuation in serpentinite and amphibole, *J. Geophys. Res.*, *102*(B2), 3051–3065, doi:10.1029/96JB03392.

Kincaid, C., and R. W. Griffiths (2004), Variability in flow and temperatures within mantle subduction zones, *Geochem. Geophys. Geosyst.*, *5*, Q06002, doi:10.1029/2003GC000666.

Kincaid, C., and I. S. Sacks (1997), Thermal and dynamical evolution of the upper mantle in subduction zones, *J. Geophys. Res.*, *102*(B6), 12,295–12,315, doi:10.1029/96JB03553.

Kutterolf, S., A. Freundt, and W. Perez (2008), Pacific offshore record of plinian arc volcanism in Central America: 2. Tephra volumes and erupted masses, *Geochem. Geophys. Geosyst.*, *9*, Q02S02, doi:10.1029/2007GC001791.

Langmuir, C. H., E. M. Klein, and T. Plank (1992), Petrological systematics of mid-ocean ridge basalts: Constraints on melt generation beneath ocean ridges, in *Mantle Flow and Melt Generation at Mid-Ocean Ridges*, *Geophys. Monogr. Ser.*, vol. 71, edited by J. Phipps-Morgan et al., pp. 183–280, AGU, Washington, D. C.

Langmuir, C., A. Benzos, S. Escrig, and S. Parman (2006), Chemical systematics and hydrous melting of the mantle in back-arc basins, in *Back-Arc Spreading Systems - Geological, Biological, Chemical, and Physical Interactions*, *Geophys. Monogr. Ser*, vol. 166, edited by D. Christie et al., pp. 87–146, AGU, Washington, D. C.

Leeman, W. P., M. J. Carr, and J. D. Morris (1994), Boron geochemistry of the Central American volcanic arc; constraints on the genesis of subduction-related magmas, *Geochim. Cosmochim. Acta*, *58*(1), 149–168, doi:10.1016/0016-7037(94)90453-7.

Lindsay, F. N., E. Gazel, C. T. Herzberg, M. J. Carr, and M. D. Feigenson (2006), Xenoliths of Cerro Mercedes, Costa Rica: A geochemical record of arc history?, *Eos Trans. AGU*, *87*(52), Fall Meet. Suppl., Abstract V51F–04.

MacKenzie, L. A., G. A. Abers, and K. M. Fischer (2008), Crustal structure along the southern Central American volcanic front, *Geochem. Geophys. Geosyst.*, *9*, Q08S09, doi:10.1029/2008GC001991.

Mehl, L., B. R. Hacker, G. Hirth, and P. B. Kelemen (2003), Arc-parallel flow within the mantle wedge: Evidence from the accreted Talkeetna arc, south central Alaska, *J. Geophys. Res.*, *108*(B8), 2375, doi:10.1029/2002JB002233.

Morris, J. D., W. P. Leeman, and F. Tera (1990), The subducted component in island arc lavas: Constraints from Be isotopes and B-Be systematics, *Nature*, *344*, 31–35, doi:10.1038/344031a0.

Myers, S. C., S. Beck, G. Zandt, and T. Wallace (1998), Lithospheric-scale structure across the Bolivian Andes from tomographic images of velocity and attenuation for P and S waves, *J. Geophys. Res.*, *103*(B9), 21,233–21,252, doi:10.1029/98JB00956.

Nakajima, J., and A. Hasegawa (2003), Estimation of thermal structure in the mantle wedge of northeastern Japan from seismic attenuation data, *Geophys. Res. Lett.*, *30*(14), 1760, doi:10.1029/2003GL017185.

Nakajima, J., Y. Takai, and A. Hasegawa (2005), Quantitative analysis of the inclined low-velocity zone in the mantle wedge of northeastern Japan: A systematic change of melt-filled pore shapes with depth and its implications for melt migration, *Earth Planet. Sci. Lett.*, *234*, 59–70, doi:10.1016/j.epsl.2005.02.033.

Park, J., C. R. Lindberg, and F. L. Vernon (1987), Multitaper spectral analysis of high-frequency seismograms, *J. Geophys. Res.*, *92*(B12), 12,675–12,684, doi:10.1029/JB092iB12p12675.

Patino, L. C., M. J. Carr, and M. D. Feigenson (2000), Local and regional variations in Central American arc lavas controlled by variations in subducted sediment input, *Contrib. Mineral. Petrol.*, *138*(3), 265–283, doi:10.1007/s004100050562.

Peacock, S. M. (1996), Thermal and petrologic structure of subduction zones, in *Subduction Top to Bottom*, *Geophys. Monogr. Ser*, vol. 96, edited by G. E. Bebout et al., pp. 119–133, AGU, Washington, D. C.

Peacock, S. M., et al. (2005), Thermal structure of the Costa Rica-Nicaragua subduction zone, *Phys. Earth Planet Inter.*, *149*(1–2), 187–200, doi:10.1016/j.pepi.2004.08.030.

Plank, T., and C. H. Langmuir (1988), An evaluation of the global variations in the major element chemistry of arc basalts, *Earth Planet. Sci. Lett.*, *90*(4), 349–370, doi:10.1016/0012-821X(88)90135-5.

Plank, T., and C. H. Langmuir (1993), Tracing trace elements from sediment input to volcanic output at subduction zones, *Nature*, *362*(6422), 739–743, doi:10.1038/362739a0.

Plank, T., C. A. Rychert, K. M. Fischer, G. A. Abers, and E. M. Syracuse (2007), Temperature of mantle melts beneath Central America: Integrating petrologic and seismic obser-



15252027, 2008, 10, Downloaded from https://agupubs.onlinelibrary.wiley.com/doi/10.1029/2008GC002040 by Cochrane Costa Rica, Wiley Online Library on [21/07/2025]. See the Terms and Conditions (https://onlinelibrary.wiley.com/terms-and-conditions) on Wiley Online Library for rules of use; OA articles are governed by the applicable Creative Commons License

vations, *Eos Trans., AGU*, *88*(52), Fall Meet. Suppl., Abstract T44C–07.

Protti, M., F. Guendel, and K. McNally (1995), Correlation between the age of the subducting Cocos Plate and the geometry of the Wadati-Benioff zone under Nicaragua and Costa Rica,in *Geologic and Tectonic Development of the Caribbean Plate Boundary in Southern Central America*, edited by P. Mann, pp. 309–326, Geol. Soc. of Am., Boulder, Colo.

Ranero, C. R., M. J. Phipps, K. McIntosh, and C. Reichert (2003), Bending-related faulting and mantle serpentinization at the Middle American Trench, *Nature*, *425*(6956), 367–373, doi:10.1038/nature01961.

Reagan, M. K., J. D. Morris, E. A. Herrstrom, and M. T. Murrell (1994), Uranium series and beryllium isotope evidence for an extended history of subduction modification of the mantle below Nicaragua, *Geochim. Cosmochim. Acta*, *58*(19), 4199–4212, doi:10.1016/0016-7037(94)90273-9.

Roggensack, K., R. L. Hervig, S. B. McKnight, and S. N. Williams (1997), Explosive basaltic volcanism from Cerro Negro Volcano; influence of volatiles on eruptive style, *Science*, *277*(5332), 1639–1642, doi:10.1126/science.277.5332.1639.

Roth, E. G., D. A. Wiens, L. M. Dorman, J. Hildebrand, and S. C. Webb (1999), Seismic attenuation tomography of the Tonga-Fiji region using phase pair methods, *J. Geophys. Res.*, *104*(B3), 4795–4809, doi:10.1029/1998JB900052.

Rupke, L. H., J. P. Morgan, H. Matthias, and J. A. D. Connolly (2002), Are the regional variations in Central American arc lavas due to differing basaltic versus peridotitic slab sources of fluids?, *Geology*, *30*(11), 1035–1038, doi:10.1130/0091-7613(2002)030<1035:ATRVIC>2.0.CO;2.

Sadofsky, S., M. Portnyagin, K. Hoernle, and P. van den Bogaard (2008), Subduction cycling of volatiles and trace elements through the Central American volcanic arc: Evidence from melt inclusions, *Contrib. Mineral. Petrol.*, *155*, 433–456, doi:10.1007/s00410-007-0251-3.

Sarker, G., and G. A. Abers (1998), Deep structures along the boundary of a collisional belt: Attenuation tomography of P and S waves in the Greater Caucasus, *Geophys. J. Int.*, *133*, 326–340, doi:10.1046/j.1365-246X.1998.00506.x.

Schlotterbeck, B. A., and G. A. Abers (2001), Three-dimensional attenuation variations in southern California, *J. Geophys. Res.*, *106*(B12), 30,719–30,735, doi:10.1029/2001JB000237.

Schmidt, M. W., and S. Poli (1998), Experimentally based water budgets for dehydrating slabs and consequences for arc magma generation, *Earth Planet. Sci. Lett.*, *163*(1–4), 361–379, doi:10.1016/S0012-821X(98)00142-3.

Schurr, B., G. Asch, A. Rietbrock, R. Trumbull, and C. Haberland (2003), Complex patterns of fluid and melt transport in the central Andean subduction zone revealed by attenuation tomography, *Earth Planet. Sci. Lett.*, *215*(1–2), 105–119, doi:10.1016/S0012-821X(03)00441-2.

Shito, A., and T. Shibutani (2003), Anelastic structure of the upper mantle beneath the northern Philippine Sea, *Phys. Earth Planet Inter.*, *140*, 319–329, doi:10.1016/j.pepi.2003.09.011.

Sinton, C. W., R. A. Duncan, and P. Denyer (1997), Nicoya Peninsula, Costa Rica: A single suite of Caribbean oceanic plateau magmas, *J. Geophys. Res.*, *102*(B7), 15,507–15,520, doi:10.1029/97JB00681.

Spiegelman, M., and D. McKenzie (1987), Simple 2-D models for melt extraction at mid-ocean ridges and island arcs, *Earth Planet. Sci. Lett.*, *83*(1–4), 137–152, doi:10.1016/0012-821X(87)90057-4.

Stachnik, J. C., G. A. Abers, and D. H. Christensen (2004), Seismic attenuation and mantle wedge temperatures in the Alaska subduction zone, *J. Geophys. Res.*, *109*, B10304, doi:10.1029/2004JB003018.

Stolper, E., and S. Newman (1994), The role of water in the petrogenesis of Mariana Trough magmas, *Earth Planet. Sci. Lett.*, *121*(3–4), 293–325, doi:10.1016/0012-821X(94)90074-4.

Syracuse, E. M., and G. A. Abers (2006), Global compilation of variations in slab depth beneath arc volcanoes and implications, *Geochem. Geophys. Geosyst.*, *7*, Q05017, doi:10.1029/2005GC001045.

Syracuse, E. M., G. A. Abers, K. Fischer, L. MacKenzie, C. Rychert, M. Protti, V. González, and W. Strauch (2008), Seismic tomography and earthquake locations in the Nicaraguan and Costa Rican upper mantle, *Geochem. Geophys. Geosyst.*, *9*, Q07S08, doi:10.1029/2008GC001963.

Takanami, T., I. S. Sacks, and A. Hasegawa (2000), Attenuation structure beneath the volcanic front in northeastern Japan from broad-band seismograms, *Phys. Earth Planet Inter.*, *121*(3–4), 339–357, doi:10.1016/S0031-9201(00)00169-2.

Tarantola, A. (1987), *Inverse Problem Theory: Methods for Data Fitting and Model Parameter Estimations*, 613 pp., Elsevier Sci., New York.

Tarantola, A., and B. Valette (1982), Generalized non-linear inverse problems solved using least-squares criterion, *Rev. Geophys.*, *20*, 219–232, doi:10.1029/RG020i002p00219.

Tatsumi, Y. (1986), Formation of the volcanic front in subduction zones, *Geophys. Res. Lett.*, *13*(8), 717–720, doi:10.1029/GL013i008p00717.

Tsumura, N., S. Matsumoto, S. Horiuchi, and A. Hasegawa (2000), Three-dimensional attenuation structure beneath the northeastern Japan arc estimated from spectra of small earthquakes, *Tectonophysics*, *319*(4), 241–260, doi:10.1016/S0040-1951(99)00297-8.

van Keken, P. E., B. Kiefer, and S. M. Peacock (2002), High-resolution models of subduction zones; implications for mineral dehydration reactions and the transport of water into the deep mantle, *Geochem. Geophys. Geosyst.*, *3*(10), 1056, doi:10.1029/2001GC000256.

von Huene, R., C. R. Ranero, W. Weinrebe, and K. Hinz (2000), Quaternary convergent margin tectonics of Costa Rica, segmentation of the Cocos Plate, and Central American volcanism, *Tectonics*, *19*(2), 314–334, doi:10.1029/1999TC001143.

Wade, J. A., T. Plank, W. G. Melson, G. J. Soto, and E. H. Hauri (2006), The volatile content of magmas from Arenal volcano, Costa Rica, *J. Volcanol. Geotherm. Res.*, *157*, 94–120, doi:10.1016/j.jvolgeores.2006.03.045.

Wallace, P. J. (2005), Volatiles in subduction zone magmas: Concentrations and fluxes based on melt inclusion and volcanic gas data, *J. Volcanol. Geotherm. Res.*, *140*(1–3), 217–240, doi:10.10216/j.jvolgeores.2004.07.023.

Walther, C. H. E. (2000), Crustal structure across the Pacific margin of Nicaragua: Evidence for ophiolitic basement and a shallow mantle sliver, *Geophys. J. Int.*, *141*(3), 759–777, doi:10.1046/j.1365-246x.2000.00134.x.

Werner, R., K. Hoernle, P. van den Bogaard, C. Ranero, R. von Huene, and D. Korich (1999), Drowned 14-m.y. -old Galapagos Archipelago off the coast of Costa Rica; implications for tectonic and evolutionary models, *Geology*, *27*(6), 499–502, doi:10.1130/0091-7613(1999)027<0499:DMYOGP>2.3.CO;2.



15252027, 2008, 10, Downloaded from https://agupubs.onlinelibrary.wiley.com/doi/10.1029/2008GC002040 by Cochrane Costa Rica, Wiley Online Library on [21/07/2025]. See the Terms and Conditions (https://onlinelibrary.wiley.com/terms-and-conditions) on Wiley Online Library for rules of use; OA articles are governed by the applicable Creative Commons License